

THE CARNEGIE-SPITZER-IMACS REDSHIFT SURVEY OF GALAXY EVOLUTION SINCE $z = 1.5$: I. DESCRIPTION AND METHODOLOGY¹

DANIEL D. KELSON², RIK J. WILLIAMS², ALAN DRESSLER², PATRICK J. MCCARTHY², STEPHEN A. SHECTMAN, JOHN S. MULCHAEY, EDWARD V. VILLANUEVA, JEFFREY D. CRANE, & RYAN F. QUADRI

The Observatories of the Carnegie Institution for Science, 813 Santa Barbara St., Pasadena, CA 91101

(Draft November 4, 2021)

ABSTRACT

We describe the Carnegie-Spitzer-IMACS (CSI) Survey, a wide-field, near-IR selected spectrophotometric redshift survey with the Inamori Magellan Areal Camera and Spectrograph (IMACS) on Magellan-Baade. By defining a flux-limited sample of galaxies in Spitzer *IRAC* $3.6\mu\text{m}$ imaging of SWIRE fields, the CSI Survey efficiently traces the stellar mass of average galaxies to $z \sim 1.5$. This first paper provides an overview of the survey selection, observations, processing of the photometry and spectrophotometry. We also describe the processing of the data: new methods of fitting synthetic templates of spectral energy distributions are used to derive redshifts, stellar masses, emission line luminosities, and coarse information on recent star-formation. Our unique methodology for analyzing low-dispersion spectra taken with multilayer prisms in *IMACS*, combined with panchromatic photometry from the ultraviolet to the IR, has yielded 37,000 high quality redshifts in our first 5.3 deg^2 of the SWIRE XMM-LSS field. We use three different approaches to estimate our redshift errors and find robust agreement. Over the full range of $3.6\mu\text{m}$ fluxes of our selection, we find typical uncertainties of $\sigma_z/(1+z) \lesssim 0.015$. In comparisons with previously published VVDS redshifts, for example, we find a scatter of $\sigma_z/(1+z) = 0.012$ for galaxies at $0.8 \leq z \leq 1.2$. For galaxies brighter and fainter than $i = 23 \text{ mag}$, we find $\sigma_z/(1+z) = 0.009$ and $\sigma_z/(1+z) = 0.025$, respectively. Notably, our low-dispersion spectroscopy and analysis yields comparable redshift uncertainties and success rates for both red and blue galaxies, largely eliminating color-based systematics that can seriously bias observed dependencies of galaxy evolution on environment.

Subject headings: galaxies: evolution — galaxies: high-redshift — galaxies: stellar content — infrared: galaxies

1. INTRODUCTION

Understanding the evolution of galaxies and large scale structure remains a fundamental challenge in astrophysics. Many ambitious galaxy surveys have been carried out to address this problem, but limited time on large telescopes results in a classic problem: sky coverage, depth, and spectral resolution – choose two. For example, the very-wide-area Sloan Digital Sky Survey (SDSS) provides a wealth of spectral information for galaxies over a cosmologically significant volume, but its modest depth limits the SDSS to the relatively local, ‘modern’ universe. Conversely, the Hubble Ultra-Deep Field photometric survey probes deep into cosmic time — to the epoch of reionization, but only over a tiny volume whose small population of galaxies leads to large uncertainties on their physical properties. While the union of such surveys has begun to paint a coherent picture of galaxy growth, significant patches of blank canvas limit our ability to fully describe how environmental processes, the infall of gas that fuels star formation, galaxy mergers and acquisitions, and feedback, all shape the evolution of galaxies over cosmic time.

The Carnegie-Spitzer-IMACS Survey (CSI) has been

designed to address one of the most dramatic and least understood features of galaxy evolution — the remarkably rapid decline in cosmic star formation since $z \sim 1.5$. It is during this extended epoch of galaxy maturation that galaxy groups and clusters have also emerged as a conspicuous feature of the landscape. The CSI Survey is uniquely able to link together the evolution of individual galaxies with these features of large-scale structure growth.

In our ambitious spectrophotometric redshift survey of distant galaxies, we strike a balance between the aforementioned three factors: (1) high completeness to moderate redshift ($z \lesssim 1.5$), (2) spectral resolution intermediate between conventional photometric and spectroscopic surveys (combining the efficiency of imaging surveys with a spectral resolution high enough to resolve large-scale structure and prominent emission-lines); and (3) an unprecedented area of 15 deg^2 for a $z \gtrsim 1$ survey. This gives the CSI Survey a volume comparable to the SDSS, with a selection method that efficiently traces stellar mass over $2/3$ the age of the universe ($0.4 < z < 1.5$) — spanning the critical redshift range where cosmic star formation precipitously drops, and groups and clusters become prominent. As the redshift survey with the largest unbiased volume at $z = 1$, CSI will allow us to comprehensively address the interplay between environment, galaxy mass buildup, and star formation at these redshifts.

In this, the first paper of the CSI Survey, we describe the design of the project, with particular focus on the flux

¹ This paper includes data gathered with the 6.5 meter Magellan Telescopes located at Las Campanas Observatory, Chile.

² Visiting Astronomer, Kitt Peak National Observatory, National Optical Astronomy Observatory, which is operated by the Association of Universities for Research in Astronomy (AURA) under cooperative agreement with the National Science Foundation.

limits of the selection, the data processing and the spectral energy distribution (SED) fitting with its attendant determination of redshifts and redshift errors. We apply our methodologies to the first batch of data in 5 deg^2 of the SWIRE XMM-LSS field, and provide an overview of some basic properties of galaxies over the past 9 Gyr, with an emphasis on the gains made by selecting galaxies by stellar mass instead of by their rest-frame UV light.

2. THE CARNEGIE-SPITZER-IMACS SURVEY

2.1. *The limitations of optically-selected surveys*

Any effective probe of galaxy assembly must sample a wide range of masses in order to trace evolutionary connections between large and small systems. The build-up of massive red sequence galaxies may be driven by mergers with sub- M^* systems, so it is essential to trace evolution to masses below M^* to mitigate against the differential growth of the high- and low-mass populations. This trade-off between depth and area noted above has led to a dichotomy in redshift surveys. Very deep programs, such as the Gemini Deep Survey (GDDS; Abraham et al. 2004) or the Galaxy Mass Assembly Ultra-deep Spectroscopic Survey (GMASS; Halliday et al. 2008) could not cover enough volume to robustly sample the evolution of the high mass population at $z < 1$, while other surveys that have traded depth for area do not reach below M^* with high fidelity.

An old stellar population at $z = 1$ with a stellar mass of $10^{11} M_{\odot}$ corresponds to roughly $i = 23$ mag and $r = 24$ mag in the optical, as shown in Figure 1 (top left). The extreme optical faintness of such galaxies results in many of them being missed in optically-selected surveys despite their relatively high masses. For example, the selection limits for DEEP2 (Willmer et al. 2006) and PRIMUS (Coil et al. 2010) are shown in this figure by the blue and green dashed lines, respectively. At $z > 1$ these programs *required* galaxies to be extremely massive or have their optical light dominated by young stellar populations in order to be fall within the survey selection. At best it can be difficult to trace the evolution of the most massive galaxies with such surveys. At worst, if not properly accounted for, color-dependent selection effects introduce biases and systematic effects. Extremely deep optical limits can be taken as one valid approach to ameliorating this problem, with the side effect of an overwhelming number of low-mass star-forming dwarfs dominating one’s source catalog.

2.2. *The potential of an IRAC-selected survey*

The integrated light of all but the youngest stellar populations are dominated by light from the stellar giant branch, cool stars whose light output peaks in the near-IR. It has long been recognized (e.g., Wright et al. 1994) that this results in a $1.6\mu\text{m}$ “bump” – a peak in bolometric luminosity – for galaxies with a wide range of star formation histories. Indeed, as shown clearly in (for example) Figure 1 of Sorba & Sawicki (2010), this feature is nearly unchanging in Bruzual & Charlot (2003) models of stellar populations with mean ages $100 \text{ Myr} < \tau < 10 \text{ Gyr}$. Put in other terms, the near-IR mass-to-light ratio, $M/L_{1.6\mu\text{m}}$ changes slowly for all but the youngest stellar populations.

The CSI Survey exploits the wide field and sensitivity of the *Spitzer Space Telescope* with the *Infrared Array*

Camera (IRAC) to take advantage of this property of the integrated near-IR light from stellar populations in $z \sim 1$ galaxies. Combined with the insensitivity to internal and Galactic extinction, selection at $3.6\mu\text{m}$ closely mirrors selection by stellar mass. Figure 1 (top left) directly compares the evolution of $3.6\mu\text{m}$ magnitude with the optical r and i bands: the CSI selection wavelength has a dependence on redshift that is much shallower than surveys selected in the optical. What slope remains for the CSI selection function is the unavoidable *k-correction*: over the redshift range $0.7 < z < 1.5$, the center of the $3.6\mu\text{m}$ IRAC band corresponds to restframe wavelengths of $2.1\mu\text{m} > \lambda_c > 1.4\mu\text{m}$, that is, straddling the $1.6\mu\text{m}$ “bump” of the spectral energy distribution (SED), but shifting through this feature as the redshift changes.

Even so, massive galaxies exhibit a much flatter trend of observed magnitudes with redshift in the IR than in the optical, and this weaker dependence on galaxy mass afforded by $3.6\mu\text{m}$ -selection of the sample is a key feature of the CSI Survey. Our goal has been to make a spectrophotometric survey to characterize the galaxy populations and environments to $z = 1.5$, unbiased at all redshifts down to a stellar mass of $M = 4 \times 10^{10} M_{\odot}$. As can be read from Figure 1, this mass limit corresponds at $z = 1$ to $r = 25$ mag or $i = 24$ mag, with equivalent limits of $r = 26$ mag and $i = 25$ mag to reach this mass limit at $z = 1.2$. Our current spectroscopic reduction and analysis, described below, is reaching an effective photometric limit of $r = 26$ mag (the dashed orange line).

Figure 1 (bottom left) plots the limiting mass as a function of redshift for CSI (solid orange) and other redshift surveys. The depth of CSI in stellar mass is substantially less sensitive to redshift compared to the others due to the IRAC $3.6\mu\text{m}$ selection, varying by a factor ~ 3 over $z = 0.5 - 1.5$, compared to $1 - 2$ dex over the same redshift range for optically-selected surveys. The result is that CSI samples nearly uniformly by stellar mass for the full, large volume of the survey, and to a lookback time of 9 Gyr.

This critical point is illustrated in Figure 1 (bottom right), plotting the depth in stellar mass against the volume probed with complete, unbiased samples. DEEP2, shown in violet (the line colors are the same as in the bottom left), is limited in both area and mass depth. PRIMUS’s 9 deg^2 is limited in depth, and thus only probes an unbiased volume comparable to our first 5 deg^2 . When CSI reaches its goal of 15 deg^2 , the survey will cover an unbiased volume equal to the SDSS with similar depth in stellar mass. The large areas available from legacy Spitzer IRAC surveys — both wide *and* deep, and the freedom from foreground and internal extinction at this wavelength, allows the construction of uniformly deep, homogeneous photometric samples for spectroscopic follow-up.

CSI reaches factors of 2-6 deeper than DEEP2 in mass, over an area ultimately 8 times wider, and redshifts sufficiently accurate to characterize environments by directly identifying groups and clusters. With such data we aim to make the first group catalog at $z = 1$ that is statistically comparable to SDSS, and thus enable the first detailed environmental characterizations of galaxies at a time when the universe was less than half its current age.

In this first paper, we describe the details of our

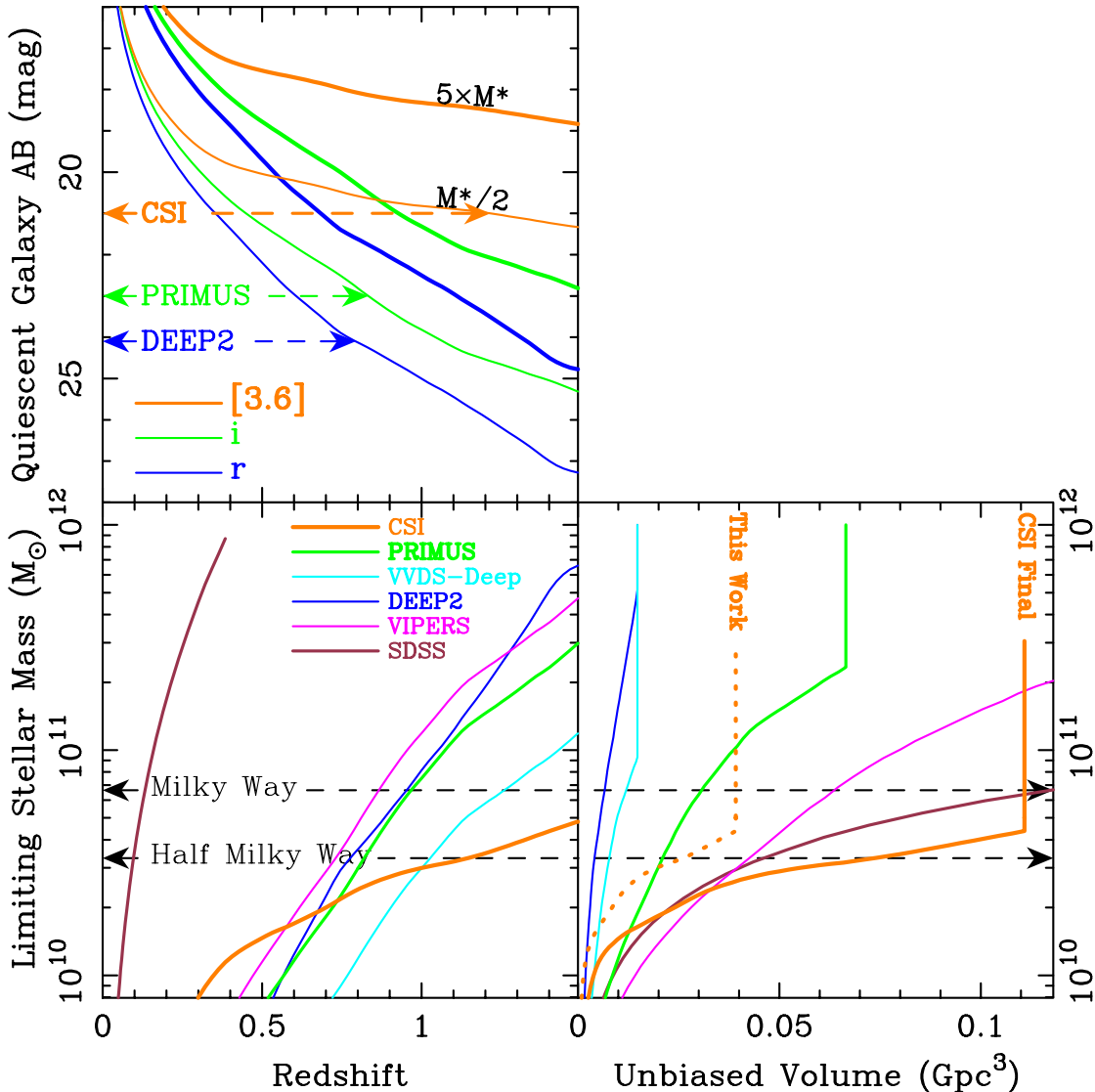


Figure 1. (top left) Apparent magnitudes in r , i , and $3.6\mu\text{m}$ as a function of redshift, for passively evolving stellar populations ($3 \leq z_f \leq 6$) with stellar masses $5M^*$ and $M^*/2$ ($\log M^* \sim 10.85$ at $z \lesssim 1$; Drory et al. 2009). The magnitude limits for DEEP2 (Willmer et al. 2006) and PRIMUS (Coil et al. 2010) are drawn. Such optical flux limits only cover the most massive passively evolving systems or those galaxies with young unattenuated stellar populations, biasing galaxy samples at early times. The shallow dependence of the $3.6\mu\text{m}$ magnitude on redshift yields a selection with significantly less bias against old systems. (bottom left) Limiting stellar mass of faint galaxy surveys by redshift. By using the *IRAC* $3.6\mu\text{m}$ band, the CSI survey (the solid orange line) traces stellar mass more uniformly than samples selected in the optical. Our sample reaches stellar masses equivalent to the present day Milky Way ($6.6 \times 10^{10} M_\odot$; McMillan 2011) out to $z = 1.4$, almost order-of-magnitude lower than DEEP2, and half the present day Milky Way at $z = 0.9$, a factor of two deeper than DEEP2 or PRIMUS. (bottom right) Volumes probed with complete, unbiased samples for several redshift surveys as functions of limiting stellar mass. When the 15 deg^2 is completed, CSI’s volume will be more than an order of magnitude larger than DEEP2. The volume traced by the first 5.3 deg^2 (this paper) is shown by the dotted line.

data reduction and redshift fitting, redshifts for the first 37,000 galaxies in 5.3 deg^2 of the SWIRE-XMM field (Figure 2), and an initial characterization of the general galaxy populations in our stellar mass-limited sample.

3. DATA

A project of this type and scope requires attention to detail and care in the processing of a broad range of data from different sources. In this section we describe the imaging data and reductions that underpin the broadband flux measurements for the sample, both for the ultimate goal of fitting SEDs, but also for defining the selection criteria and incompleteness functions. Unless otherwise specified, all object detection was performed

using SExtractor (Bertin & Arnouts 1996).

3.1. Photometry

The SWIRE Legacy Survey (Lonsdale et al. 2003) observed several large fields with *IRAC* to a depth suitable for our survey. Three of these fields are accessible from southern telescopes, providing up to 23.8 deg^2 of coverage at $3.6\mu\text{m}$. Basic properties of the three fields are given in Table 1. Of these fields, 15.3 deg^2 have supplemental optical imaging that is publicly available. Of the 9.1 deg^2 of *IRAC* imaging in the XMM-LSS field, 6.9 deg^2 is covered by the CFHT Legacy Survey W1 *ugriz* imaging. In this section we discuss our analysis of the SWIRE XMM-LSS *IRAC* data, our reprocessing

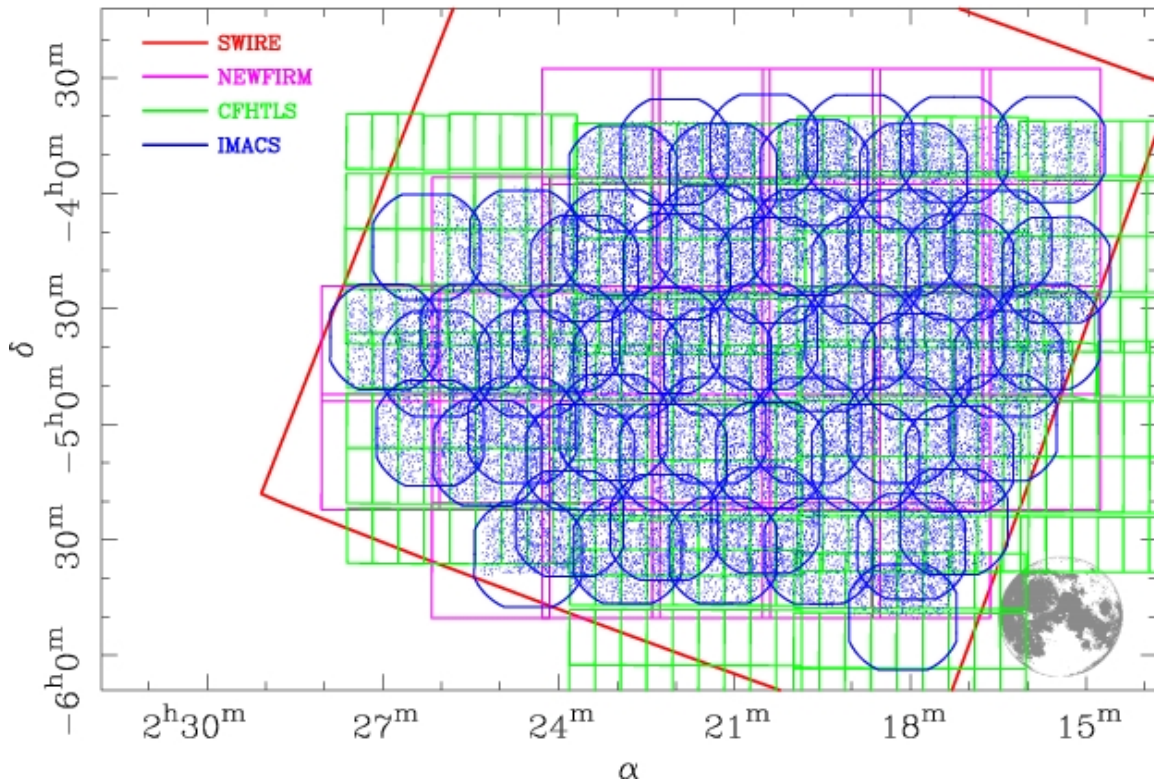


Figure 2. A schematic of observations in the first 5 deg² of the SWIRE-XMM field studied by the Carnegie-Spitzer-IMACS survey. The SWIRE *IRAC* imaging field is outlined in red. The CFHTLS-W1 optical data reanalyzed by us is shown in green. The first set of NEWFIRM *J* and *K_s* observations are marked in violet. The positions of the IMACS slitmasks are outlined in blue, with the blue points marking the positions of the 37,000 galaxies with CSI redshifts. The field of view of IMACS is comparable to the size of the full moon, illustrated in the lower right.

of the CFHTLSW1 *ugriz* imaging and subsequent photometry of the 3.6 μ m catalog, as well as our observations at *J* and *K_s* of the field using NEWFIRM (Autry et al. 2003) on the Mayall 4m telescope at Kitt Peak National Observatory.

3.1.1. Spitzer-IRAC Imaging

The SWIRE Legacy Survey was a program undertaken to trace galaxies by stellar mass back to $z = 2$ (Lonsdale et al. 2003). The *IRAC* images of the XMM-LSS field were obtained from the archive at IPAC. The reductions and processing of these data were described by Surace et al. (2005). In order to minimize contamination of the object catalog by artifacts around stars, we configured SExtractor so as to ignore elliptical regions around bright stars. A ‘mexican hat’ convolution kernel was used for object detection, resulting in 585,159 objects in the 3.6 μ m catalog of the XMM-LSS field. Fluxes were measured in a manner described by Surace et al. (2005). Down to our selection limit of 3.6 $_{AB} = 21$ mag the 3.6 μ m catalog contained 266,621 objects.

3.1.2. The Optical Imaging

The CFHT Legacy Survey (Cuillandre & Bertin 2006) targeted multiple fields using the one-degree MegaCam imager around the sky with a broad range of scientific goals. The ‘Wide’ survey focused on several astrophysical questions, with the W1 field providing almost 7 deg² of overlapping *ugriz* coverage in the SWIRE XMM-LSS field. Unfortunately, the processed images and catalogs available at Terapix were not entirely suitable for our

Table 1
Basic Properties of the Southern SWIRE Fields
Targeted by CSI

Field	SWIRE Area (degs ²)	SWIRE+Optical (degs ²)	Filters
XMM-LSS	9.1	6.9	<i>ugriz</i>
ELAIS S1	6.9	3.6	BVR <i>Iz</i>
CDFS	7.8	4.8	<i>ugriz</i>

purposes, owing to uncertain astrometry and improper defringing of the *i* and *z* data. Therefore, we obtained the complete set of calibrated frames from the CFHT archive and processed the data using the following additional steps. First, we constructed new fringe frames in *i* and *z* by medianing scaled exposures obtained within a single night. These were then rescaled and subtracted from the individual exposures. Some bright objects did bias these medians when the number of exposures was small (i.e. $N \lesssim 10$), leaving faint traces in the resulting fringe frames. In general, however, the greater sky uniformity after subtraction of these new fringe frames improved the depth of our resulting catalogs by ~ 0.2 to 0.5 mag compared to the on-line catalogs. We constructed sky frames as well for the *u*, *g*, and *r* bands using a similar methodology, though not restricting the construction to data collected within single nights.

New astrometric solutions were derived for each exposure using the *IRAC* catalog as a set of deep astrometric standards. Cubic solutions for each chip were

derived with a typical RMS scatter of $0''.15$. For those regions of the MegaCam images that did not overlap the SWIRE data, we supplemented the catalog with the 2MASS point source catalog (Skrutskie et al. 2006), in order to prevent the solutions from diverging at the edges of the *IRAC* field.

Using these new astrometric solutions, and the photometric solutions from the headers of the individual frames, we constructed cosmic-ray-cleaned image stacks with $0''.185$ pixels, 30 arcmin on a side and evenly spaced. These smaller images were more easily managed than the larger image formats provided by Terapix, which allowed us to distribute the image analysis and photometry tasks over multiple processors. The zeropoints were checked by comparing the photometry of moderately bright objects with the data in the catalogs from Terapix and we found systematic offsets less than ± 0.03 mag in every case. Object catalogs were generated using SExtractor, and these were matched to the *IRAC* catalog with a tolerance of $1''.5$ arcsec, with the goal of using the optical image characteristics to aid in star/galaxy separation, and to determine which *IRAC*-selected objects have centroids with optical centers falling far from the defined slit positions.

3.1.3. The Near-IR Imaging

NEWFIRM (Autry et al. 2003) is a wide-field ($27' \times 27'$) near-IR camera deployed by NOAO at the Mayall 4m at Kitt Peak from 2007 to early 2010. During the fall semesters we imaged the XMM-LSS field in *J* and *K_s*. Typical exposure times were 70 min/pixel in *J* and 32 min/pixel in *K_s*. The seeing ranged between 0.8 – 1.4 arcsec (FWHM).

The data were processed using a fully automated, custom pipeline, written as a prototype for a wide-field imager being deployed at Magellan. The basic steps in the reduction were: (1) subtraction of the dark current; (2) correction for nonlinearity; (3) division by a flat-field; (4) masking of known bad pixels; (5) construction of first-pass sky frames; (6) derivation of image shifts, in arcsec, on the sky; (7) stacking of the first-pass sky-subtracted frames; (8) generation of a deep object catalog; (9) construction of object and persistence masks for second-pass sky estimation; (10) temporary interpolation over objects, persistence, and bad pixels for each frame; (11) constructing bivariate wavelet transforms of these masked frames; (12) fitting the time variation of the wavelet transforms of the sky using shorter frequencies for larger spatial scales; (13) reconstruction of model sky frames by inverting the temporally smoothed wavelet transforms; (14) subtraction of the model sky frames; (15) re-derivation of image shifts, in arcsec, on the sky; (16) final stacking of the sky-subtracted frames, including the generation of sigma and exposure maps; (17) identification of objects in the 2MASS point source catalog, restricted by 2MASS PSC quality flags; (18) application of rotation, translation, and scale to the camera distortion based on the 2MASS objects; and (19) calculation of image zero-points using the 2MASS objects.

Using the zeropoints of each image, we constructed image mosaics $30'$ on a side centered at the locations of our *ugriz* mosaics, but with $0''.4$ pixels.

3.2. Aperture Photometry

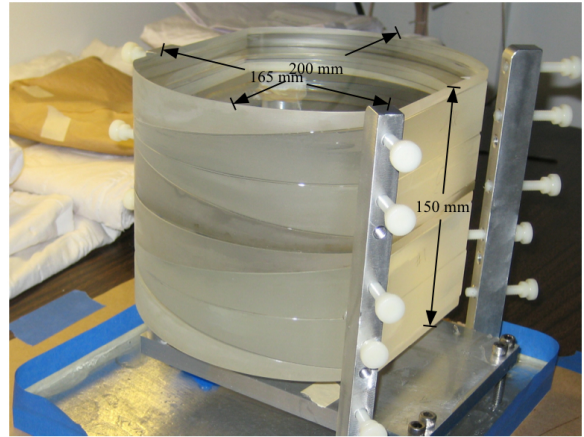


Figure 3. Construction of the new “Uniform Dispersion Prism,” built for CSI. Dr. S. Shectman designed the UDP to have a resolution of $R \sim 25$ from 7500\AA to $1\mu\text{m}$. The eight layers are made from thin prisms of S-FPL51 and N-KZFS2, to make a stack of glass 150 mm thick. This prism has a resolution with a mild dependence on wavelength (see Figure 4) compared to the first prism deployed in IMACS (see Coil et al. 2010).

Magnitudes in *ugrizJK_s* were derived using aperture photometry within a range of circular apertures for the entire SWIRE catalog. Because the seeing varied with wavelength and pointing, we convolved the *z*-band image stacks with Gaussians to simulate the effects of poorer seeing in the *ugrizJK_s* data. The offsets in magnitude from the degraded *z* images were applied as PSF-corrections to the *ugrizJK_s* aperture magnitudes. While the details of the PSF and potential blending are critical for small apertures and for modeling the profiles of the objects, our choice of fitting the SEDs to much larger-aperture ($D = 4''$) magnitudes allows us to utilize a simple and economical approach to the PSF corrections. This choice was especially important given the enormous size of the object catalog, while reducing the systematic errors in matching the aperture magnitudes to the *IRAC* $3.6\mu\text{m}$ fluxes.

3.3. Spectroscopy

Between 2008 and 2009 the SWIRE XMM field was targeted in 31 multislit mask exposures with the *IMACS* $f/2$ camera configuration and the Low Dispersion Prism (LDP) designed by S. Burles for the PRIMUS redshift survey (Coil et al. 2010). In 2010 we observed 29 SWIRE XMM masks using an innovative eight-layer disperser called the Uniform Dispersion Prism (UDP, see Figure 3). Although both of these dispersers produce spectra with median resolutions of $\lambda/\Delta\lambda \sim 30$, the dispersion curve of the UDP is much flatter, providing significantly higher resolution out to $1\mu\text{m}$ than the LDP at the expense of marginally lower resolution in the blue (Figure 4).

Previous work by the PI on a similar program had obtained adequate *S/N* ratios with exposure times of 3 hours down to $z' = 23.3$ mag using less sensitive SITE detectors (Patel et al. 2009ab, 2010, 2011). Significantly more sensitive E2V detectors were installed in *IMACS*, thanks to support from the NSF’s TSIP program (see Dressler et al. 2011); these CCDs boosted the throughput of the instrument by factors of 2-3 in the far red. We observed with these detectors using the Nod and Shuffle mode of *IMACS* (see Glazebrook & Bland-Hawthorn

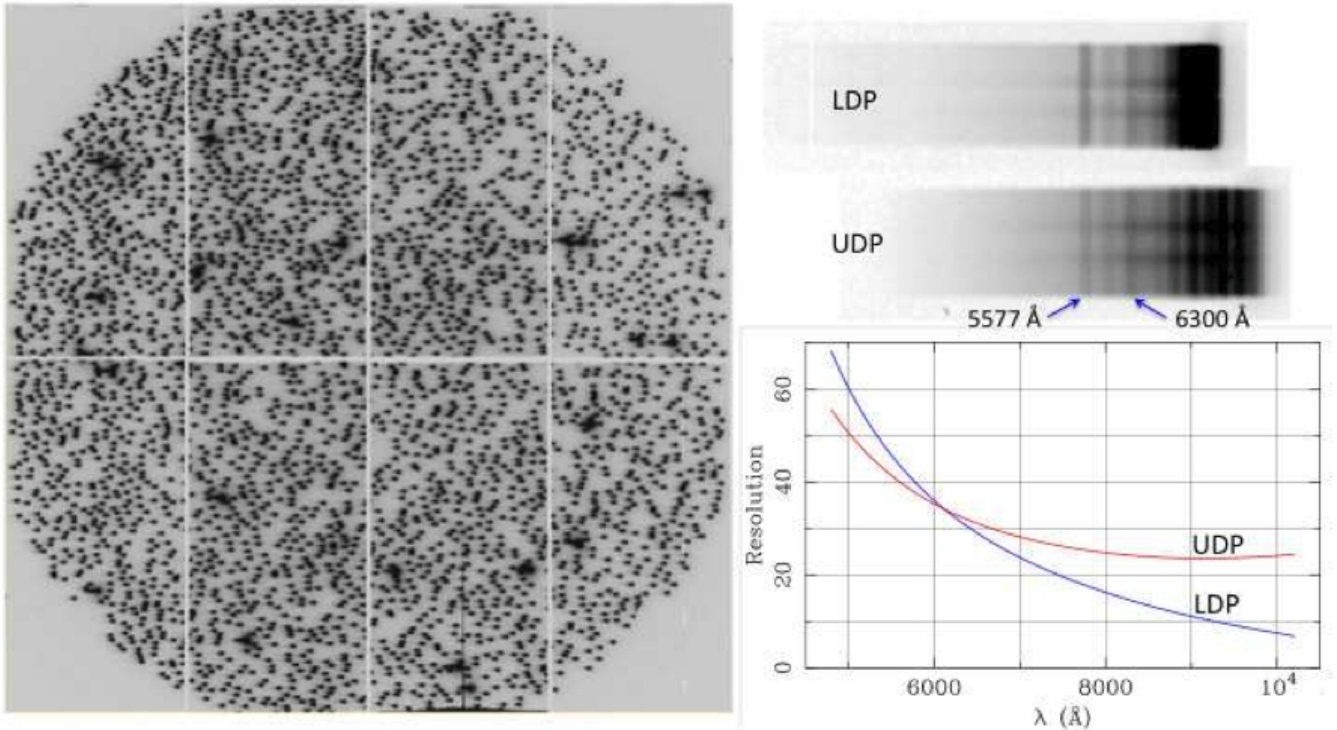


Figure 4. (Figure reproduced from Dressler et al. 2011) (left) Multi-slit mask designed for use with the Low Dispersion Prism. (top right) Example LDP spectrum — nod & shuffle (Glazebrook & Bland-Hawthorn 2001) produces doubled object and sky spectra. Night sky lines [O I]5577Å and [O I]6300Å are marked. Below the LDP spectrum is one obtained with the UDP, with its more uniform dispersion (bottom right). The resulting difference in resolution is shown in the bottom right. The resolution provided by the new Uniform Dispersion Prism, designed for CSI, provides an improved ability to trace the 4000Å break and [OII]3727Å to $z = 1.4$ when coupled with IMACS’s red sensitive e2v detectors.

2001), and accumulated exposure times of 2h per galaxy for more than 90% of the sample, using individual integrations with durations of 30 min (15 min per position). Typical slit lengths were 5 arcsec. The positions of the slit masks are shown in Figure 2.

Spectrophotometric standards were obtained during most observing runs, with a consistency of 5% from run-to-run. Helium calibration lamps illuminating the deployable flat-field screen were taken approximately every hour (i.e., every other science exposure). In this section we describe the basic steps involved in reducing the multislit prism data using the custom pipeline that had been written for the earlier cluster programs (e.g. Patel et al. 2009a,b, 2011).

3.3.1. Wavelength Calibration

Two critical aspects of the reduction of low-dispersion prism data involve mapping wavelengths on the detector, and transposing between sky coordinates of objects and CCD coordinates. Too few calibration lamp lines can be used to define the solution for a given slitlet, so we derive global wavelength mappings over an entire CCD using all of the slitlets simultaneously. Thus, lines in a single spectrum that may be corrupted by bad columns or pixels will not affect the solution for that slitlet, as the ~ 3000 helium lines over a CCD frame constrain the fit.

The following are the basic, automated steps we have implemented in our pipeline:

- Derive mapping of sky coordinates to CCD coordinates using an image of the slitmask;

- Identify lines and fit 2D wavelength solutions using isolated helium lamp exposures on a chip-by-chip basis;
- Refit new centroids for blended helium lines using nonlinear simultaneous Gaussian fitting on a slit-by-slit basis;
- Fit for improved mapping of 2D wavelength solutions;
- Shift the wavelength maps using 2-3 night sky emission lines (e.g., [O I] 5577Å, Na 5890Å, [O I] 6300Å);

We start with a distortion map for the camera, defined from previous exposures of the field around the globular cluster Palomar 5, to compute the approximate mapping of sky coordinates to CCD coordinates for the objects in the multislit mask. SExtractor is run on a direct image of the slit mask and a simple pattern analysis matches up the predicted positions of the slits and the measured positions of the slits to create an adjusted mapping of sky coordinates to CCD coordinates.

With a theoretical dispersion curve for the prism, we generate a trivariate mapping of sky coordinates to CCD coordinates that is wavelength dependent. SExtractor is run on a helium comparison lamp image and the resulting catalog of the 3,000 to 4,000 helium lines is pattern-matched to the predicted positions of 8 unblended helium lines (out of the 11 lines in our line list). New wavelength mappings are solved for as the order of the fit is

gradually increased. The nearly final solutions generated at this stage are first order rescalings of the theoretical dispersion, with coefficients that are cubic (check!) polynomials of the sky coordinates. The typical RMS at this stage is 0.4 pixels (check). With these solutions, we can now generate predicted positions for the complete helium line list and fit Gaussian profiles to the full line list for each slit. Within each slit, the Gaussians are fit simultaneously, providing accurate positions for both the unblended and blended helium lines. Using these new positions for the helium lines in CCD coordinates, we derive through iteration, the trivariate mapping between CCD coordinates and both wavelength and sky positions, with a typical final RMS scatter of 0.25 pixels. For LDP data this scatter corresponds to $\sim 50 \text{ \AA}$ at 9000 \AA , or $\delta z \sim 0.005$. This large uncertainty in the wavelength calibration in the far red is due to the fact that the dispersion reaches $\sim 200 \text{ \AA}/\text{pixel}$ at 9000 \AA ; the scatter of $\sim 50 \text{ \AA}$ introduces a 25% uncertainty in $\Delta\lambda$ at such wavelengths when computing the flux calibration. Because the resolution with the UDP is $3\times$ higher at these red wavelengths, this additional source of uncertainty is negligible for those data.

The final step involves cross-correlating simulated night sky emission lines ([OI]5577 \AA , Na I 5890 \AA , and [OI]6300 \AA) placed at their predicted positions with the spectra in the science frames, on a slit-by-slit basis. The median offset in both x and y is then applied to the wavelength mappings found from the nearest helium lamp exposure.

3.3.2. *Extracting Spectra*

Due to the unique nature of these prism data, the science frames must also be processed in a nonstandard fashion using custom written routines. We take particular care in the extraction of spectra because of the small number of pixels covered by each object, the faint optical limits we expect to probe, and the proximity of the objects to slit ends where residual sky counts can bias simple extraction algorithms. Starting with the two 2-dimensional spectra (here denoted “A” and “B”) of each galaxy that come from the nod-and-shuffle observations, the basic processing steps are as follows:

- Subtract spectrum A from B, and B from A;
- Divide by a normalized flat-field, using pixels only covered by spectrum A;
- Optimally extract each object within a given exposure, adopting a wavelength-dependent Gauss-Hermite expansion of the spatial profiles for each object, and using the pixels of the A and B spectra simultaneously;
- Solve for the global translation, rotation, and scale changes in the object positions due to slitmask misalignment;
- Fix the object positions and redo the optimal extractions, deriving new Gauss-Hermite moments and 1D spectra.
- Combine the data from all exposures of an object into a single extracted spectrum.

A more detailed description of these steps follows. Initially we subtract the night sky background spectrum, using the “B” spectrum as the sky for the “A” spectrum, and vice versa. Next we divide the results by a normalized flat-field using the pixel locations of the “A” spectrum for both “A” and “B” spectra (reminder to the reader unfamiliar with the details of Nod & Shuffle: electrons counted in the “B” pixels originated in the “A” pixels).

Recovering the one-dimensional spectra of the objects in the slitlets is now possible, but several additional steps and some care are required, because of the proximity of the objects to the ends of the slitlets, and given the relatively short nods (1.6 arcsec). Our procedure is a modification of the standard optimal extraction (Horne 1986) with several key differences. Crucially we can use both the “A” and “B” spectra simultaneously to measure the spatial profile of a given object. We employ a Gauss-Hermite decomposition of the spatial profile, with moments that are low-order Legendre polynomial functions of wavelength. An iterative routine also solves for the centroid of the Gaussian as a low-order polynomial of wavelength. The second moment (e.g., standard deviation of the Gaussian) is also determined as yet another low-order function of wavelength. A first guess for the one-dimensional spectrum of the object can be obtained using this Gaussian approximation for the spatial profile, by solving for the b-spline (Dierckx 1983) that fits the “A” and “B” data, both normalized by the wavelength-dependent Gaussian spatial profile. With this approximate spectrum, we resolve for the parameters of the spatial profile, including up to 4 Hermite moments (10 for spectrophotometric flux standards), each also wavelength-dependent. The wavelength binning of each slitlet is preserved, defined by the wavelength solution at its location.

With a first set of extracted spectra and, more importantly, object moments, in all eight CCDs of a given exposure, we analyze the difference between the predicted object positions and the detected object positions. Deviations are well described by a linear function of coordinates in the slitmask, largely the result of small misalignments when the observations were taken. We use this new linear function to fix the object positions, recompute spatial profiles, and re-extract object spectra.

Using the spatial profiles of each observation of a given object, we have a final procedure that solves for the one-dimensional spectrum using all exposures simultaneously, using the flux calibration (see below) so that all data are now in physical units. We fix the first and second moments to those determined above, and employ a similar optimal extraction routine to that described earlier, but one which uses the “A” and “B” spectra of all the exposures, recomputing the higher-order Hermite moments of the spatial profiles and solving for a b-spline that best represents the spectrum of the object in a least-squares sense. Pixels are weighted according to the inverse of the expected noise. Bad columns and flagged pixels are given zero weight. Iteration allows us to flag and reject most cosmic rays. The process performs an optimal extraction that yields a single 1D spectrum that matches all the data in a least-squares sense. Given the small differences between the wavelength solutions of the exposures, we sample the one-dimensional b-spline rep-

resentation of the spectrum at a fixed set of wavelengths, defined by the dispersion of the prism at the center of the field. This fixed grid greatly simplifies the construction of templates for fitting the SEDs.

Spectra for objects repeated in overlapping slitmasks were not combined at this stage, but kept separate — for this paper — so that we could better assess data quality and empirically estimate our redshift precision. Approximately 10% of the galaxies were repeated; we discuss these below in the context of the redshifts and their uncertainties. Approximately 20% of the objects observed with the LDP were also reobserved with the UDP.

3.3.3. Spectrophotometric Flux Calibration

Accurate flux calibration of the spectra is a critical component of the survey because the relative slope of a spectrum provides useful information for the determination of redshift. For CSI we choose bright hydrogen white dwarf standard stars with deep, broad Balmer lines that can be detected with the LDP/UDP. Deep Balmer lines are required because we expose these stars in the alignment star boxes and the positions of the absorption lines allow us to refine the zeropoints of the wavelength calibrations for the stars when they are not accurately centered in the boxes.

The processing of standard star exposures is similar to that described above, with the following modifications. First, to capture essentially all of the photons from the star, we place it in the center of an alignment star box on one of our slitmasks. By doing so we can infer the wavelength calibration for the alignment star box by using the trivariate wavelength solution of the helium lamp exposure obtained immediately after the standard star.

In order to derive the sensitivity function, we must first compensate for the fact that the seeing in the standard star exposure leads to different resolution than one would obtain with a narrow slit. We make an assumption that the seeing was isotropic and that the Gauss-Hermite parameterization of the spatial profile is a valid descriptor of the seeing profile in the dispersion direction. Using this profile as a kernel, we deconvolve the extracted spectrum using an implementation of CLEAN (Högbom 1974), convolving the result to a resolution equivalent to that defined by the science data (FWHM=4.5 pixels).

Due to time and weather constraints, spectrophotometric flux standards were not obtained during every night, but the excellent run-to-run repeatability of the relative flux calibration from 8500 Å to 4500 Å for the LDP and from 9000 Å to 4500 Å for the UDP, of approximately $\pm 5\%$ allows us to use flux standards obtained on different nights or during different runs.

4. SED FITTING

With flux calibrated spectra and broadband photometry in hand, a suitable library of template spectra can now be employed to estimate spectrophotometric redshifts. In this section we describe the basis functions in our templates, implement a generalized maximum likelihood method and estimate confidence limits for the redshifts of each galaxy along with several other parameters and properties.

Here we discuss the construction of the templates, using several continuum components, each derived from the

Maraston (2005) models. The Kroupa (2001) initial mass function (IMF) was used, resulting in a median offset from “diet” Salpeter IMF (Bell & de Jong 2001) of 0.04 dex for SSP ages up to about 9 Gyr.

4.1. Ingredients

Ideally, a set of spectral templates should not only span the broad range of redshifts a survey may probe, but also encompass the potential range of optical and near-IR properties of galaxies over those epochs. Satisfying this latter constraint cannot be done *a priori* as it is one of the chief goals of the project. However, models of evolving stellar populations have been used for modeling low-dispersion prism data for the purpose of recovering redshifts to $z \sim 1$ (see Patel et al. 2010). Our method for CSI echoes that approach, and we describe it here.

Our templates are constructed as the superposition of several continuum components and multiple emission lines. The stellar population bases were derived from the Maraston (2005) models, using the Kroupa (2001) initial mass function (IMF)³. In building our templates we exploit the well known fact that for times $\tau \gtrsim 1$ Gyr after the cessation of star formation, optical flux no longer provides significant leverage on a galaxy’s prior star formation history (Tinsley 1974). We adopt a simple set of stellar population basis functions: these components are sensitive to different timescales of a galaxy’s star formation history; in combination, they reproduce the broad range of SED properties seen in normal galaxies.

The first base component is a constant star formation model with a starting epoch of $z_f = 5$. The time at which star formation ceases for this component is a free parameter our analysis, a grid of values ranging from 10^9 yr to 10^{10} yr prior to the redshift of observation (capped at $z = 5$), whose values are spaced logarithmically with an interval of 0.10 dex. The metallicity of this base population is also gridded with values ranging from $[Z/H] = -1.2$ to $[Z/H] = 0.6$, with an interval of 0.2 dex. Redshift is the final gridded parameter, ranging from $z = 0.005$ to $z = 2.0$ at intervals of $\Delta z = 0.005$. Superimposed on the base population are up to five piecewise constant SFR populations that formed in 200 Myr intervals centered on lookback times of $t = 1, 3, 5, 7, 9 \times 10^8$ yr, with the same metallicity as that of the base. Four cartoon star formation histories built out of such components are schematized in Figure 5. The SEDs of each of these stellar components are redshifted, convolved to the wavelength-dependent resolution of the instrument, and sampled at the wavelengths appropriate for the galaxy spectra. Lastly, these are all replicated with extinctions of $A_V \in \{0.0, 0.5, 1.0, 2.0\}$ mag in an effort to reproduce the effects of complexity in the geometries of dust attenuation than simple screen models.

In addition to the continuum components, we include several emission line components: (1) a single unresolved Gaussian emission line for [OII]3727 Å, (2) a blend of three Gaussians at [OIII]5007 Å, [OIII]4959 Å, and H β 4861 Å, with ratios of 1 : 1/3 : 1/10, to broadly mimic the typical line ratios seen in galaxies at the masses we expected (e.g. Kauffmann et al. 2003), (3) a Gaussian

³ This is equivalent to applying an offset of -0.04 dex to the stellar M/L ratios of “diet” Salpeter IMFs (Bell & de Jong 2001) for single stellar population (SPP) ages up to about 9 Gyr.

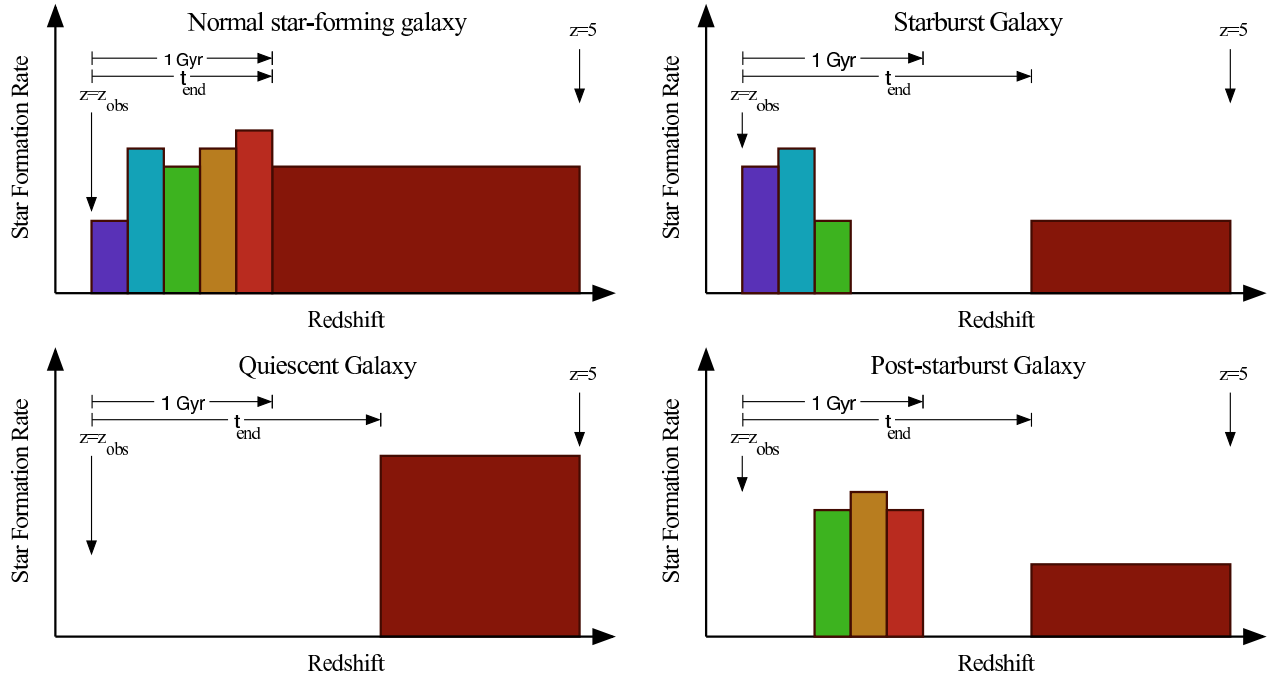


Figure 5. Cartoon star formation histories for four representative galaxy types. Because optical passbands provide poor leverage on star formation histories earlier than 1 Gyr prior to the epoch of observations, we have reduced the complexity of galaxy star formation histories to nonnegative combinations of discrete components such as those illustrated in these cartoons. For our purposes, each galaxy is modeled with six age-related components, as described in the text, with the oldest component starting at $z = 5$ and continuing down to some time t_{end} prior to the epoch of observation. Five younger, discrete components of duration 200 Myr allow for the broad possible range of complex histories in a galaxy’s recent past. Each of these six components is quadrupled, with four different levels of extinction, $A_V \in \{0, 0.5, 1, 2\}$ mag, leading to a total of 24 stellar components with non-negative contributions to the stellar mass of a galaxy. With redshift, metallicity, and t_{end} as our gridded parameters, there are 24 stellar coefficients at each location in the grid. By abstracting star formation histories in this way, we have retained the essential information content of on-going star formation, intermediate-age populations, and an old, underlying stellar population.

for H α 6563 Å, and (4) an unresolved emission line for MgI2799 Å. Because of the increasing uncertainties in the flux calibration of LDP data beyond 8000 Å, no emission lines were allowed beyond that point in those fits. Given the higher quality of the UDP data in the far red, we extended this limit to 9000 Å in fitting UDP data, with the exception of [OII]3727 Å, which we accepted to 9400 Å. These restrictions do not greatly affect the redshifts that are measured, but they do have some impact on the fit to the red continua of low redshift galaxies. Note that the widths of the Gaussian profiles are fixed to that defined by the spectral resolution.

Thus there are in total 24 stellar continuum components and 4 emission line components, each redshifted, convolved to the wavelength-dependent resolution of the instrument, and sampled at the wavelengths appropriate for the galaxy spectra. The broadband magnitudes of each component are computed using the filter transmission and detector QE curves of the respective imaging instruments.

4.2. Fitting for the Galaxy Components

Before solving for the 28 coefficients at every location in the three-dimensional grid of redshift, metallicity, and termination time, we compute a simple constant rescaling of the IMACS spectrum to the broadband *griz* photometry from the $D = 4$ arcsec aperture. In general the colors of the IMACS spectra agreed within $\pm 10\%$ of the

colors derived from the broadband photometry and adjusting for any color offset did not significantly affect the measured redshifts.

Standard least-squares and χ^2 minimization techniques are susceptible to bad data points and outliers, for example, from a few residual cosmic rays or unidentified bad pixels, especially given the small number of usable pixels in each spectrum (~ 150). We opted to perform an iteratively reweighted non-negative least squares fit for the coefficients of the template fit at each location in the grid, using the weight function of Huber’s M-estimator (Huber 1981; Zhang 1997). Doing so is equivalent to minimizing Huber’s M-estimator itself, given as L_{Huber} , with the associated weight function W_{Huber} :

$$L_{Huber}(x) = \begin{cases} x^2/2 & \text{if } |x| \leq k \\ k(|x| - k/2) & \text{if } |x| \geq k \end{cases} \quad (1)$$

$$W_{Huber}(x) = \begin{cases} 1 & \text{if } |x| \leq k \\ k/x & \text{if } |x| \geq k \end{cases} \quad (2)$$

where $k = 1.345$. Near the optimum location, points retain the behavior of $L_2 = x^2/2$ (i.e. least squares) while outside points retain the behavior of $L_1 = |x|$ (i.e. minimum absolute deviation), leading to an estimator that is robust against outliers but sensitive to the details of the distribution close to the optimum location. In three iterations the routine effectively minimized this M-estimator, instead of the L_2 M-estimator, where $L_2 =$

$\chi^2/2$. The result is a set of coefficients that are robust against any bad data present, as long as the fraction of bad pixels is $\lesssim 25\%$.

With the rescaled IMACS spectra and the *ugrizJK_s* photometry, we now solve for the template coefficients using iteratively reweighted non-negative least squares. The coefficients for each galaxy are stored, as well as several M-estimators for each grid location, for use in the final likelihood analysis (described below).

4.3. Likelihood Analysis

Each location in the three-dimensional grid of redshift, metallicity, and the termination of star-formation for the base ‘constant-star-formation’ model has a dozen coefficients, as well as goodness of fit metrics. With these grids of population coefficients and M-estimators, confidence limits on all of the gridded parameters and derived properties, such as total masses, stellar masses, restframe colors, were derived using a likelihood function

$$d\mathcal{L} = dzd \log t_{end} d[Z/H] P(z, \log t_{end}, [Z/H]) \times \exp[-L_{Huber}(z, \log t_{end}, [Z/H])] \quad (3)$$

where P is the defined set of priors at a given redshift, termination time, and metallicity. In our likelihood analysis we found that using Huber’s M-estimator gave results that were most robust to bad pixels without biasing the contributions of emission lines, though others, for example, “least-power” or “Fair” (see, e.g., Zhang 1997), were also very effective. We caution against using M-estimators that are insufficiently concave, as pixels “contaminated” by real (but narrow) features such as unresolved emission lines are attributed less weight than continuum pixels (by definition). With the three dimensional likelihood functions, and 24 SFH + 4 emission line parameters at each location in the grid, we have computed confidence limits for every parameter, and for several derived combinations of parameters such as stellar mass or a broad range of restframe colors. With these confidence limits, and a broad array of data quality measures, such as S/N ratios, minimum χ^2 , χ^2 at the peak of the likelihood function, and the confidence limits themselves, we can identify the highest quality sample possible with the current dataset.

4.4. Defining the High Quality Sample

Several criteria are used to eliminate substandard results. A number of measures were judged to be helpful, including χ^2 for the best-fit template at a given S/N ratio, the number of pixels not flagged as bad or contaminated, or unphysical inferred rest frame colors. The final criterion used to define our high quality sample was to restrict the set to those galaxies with formal 95% uncertainties in rest frame M_g of $\Delta_{95}M_g < 2.0$ mag (equivalent to $\sigma_{M_g} < 0.5$ mag). The result is a relatively clean sample of 37,000 galaxies, for which we have 44,000 spectra, over a field of 5.3 degs². For every spectrum, we have marginalized over redshift, stellar mass, rest frame colors, stellar population parameters as per the components in the SED fitting, and emission line luminosities, estimating 68%, 90% and 95% confidence intervals using the likelihood functions.

Example results of the SED fitting illustrating a broad

range of redshifts and spectral types from our high quality sample are shown in Figures 6 and 7.

Given that our sample is more effectively reaching higher redshifts at a given stellar mass than optically selected surveys such as DEEP2 and PRIMUS, we now turn to characterizing the accuracy of our redshifts.

4.5. Success Rates and Completeness

In a spectroscopic galaxy survey, the degree to which the population is sampled can be characterized by two quantities: the success rate (fraction of *targeted* galaxies for which usable spectra are obtained) and the completeness (fraction of the original *photometric* that is observed and usable spectra obtained). The latter quantity necessarily is necessary dependent on the former, and includes the effect of slit collisions. In Figures 8 (top) and (bottom) we plot success rates and completeness as functions of 3.6 μ m, i , and r magnitudes. For galaxies brighter than $r = 25.5$ mag the current pipeline produces a mean success rate of 70% and mean completeness of 38%. In detail we model the completeness as a 2D function of both 3.6 μ m magnitude and $i - [3.6]$ color, and for illustrative purposes we have overplotted the mean success rate and completeness within broad color bins (though our subsequent analysis employed finer color bins when modeling the incompleteness).

Spectroscopic surveys such as CSI that intend to study the density dependence of galaxy properties must carefully model the effect of slit collisions on the completeness. To accomplish this we divided our sample into bins based on local source density. The footprint of a CSI spectrum is ~ 200 pixels long, or 2/3 arcmin. For every target and observed galaxy, we compute the local source density within 4/9 arcmin². In Figure 8 we show the mean completeness as a function of source density computed on this scale. This monotonic function of density is taken to represent the effects of slit collisions. We have also computed the completeness functions as coarse trivariate functions of source density, [3.6] magnitude, and $i - [3.6]$ color in and found no statistically significant variation in the bivariate ([3.6], $i - [3.6]$) completeness function with source density, other than the normalization, as shown in Figure 8.

Using the trend of the mean completeness as a function of source density, and the mapping of the completeness as a bivariate function of z -band magnitude and $z - [3.6]$, we can directly multiply the two for every galaxy in the final sample. In subsequent, and relevant analysis, one can employ weights defined as the inverse of these completeness estimates. For those galaxies with multiple observations, we currently divide these weights by N_{obs} , the number of observations, though more complicated procedures may be devised at a future date. We have tested the validity of these density-dependent completeness corrections by recomputing the local source densities based on the high-quality spectroscopic sample alone. On the scales of 2/3 arcmin, the agreement is very good, with a scatter of approximately 0.3 dex. On larger scales, of 2 or 4 arcmin, the agreement is even better with scatters of < 0.1 dex at a given density. These corrections, and the accuracy with which they can reproduce the original source densities, are crucial for ensuring confidence in the galaxy group mass estimates derived below.

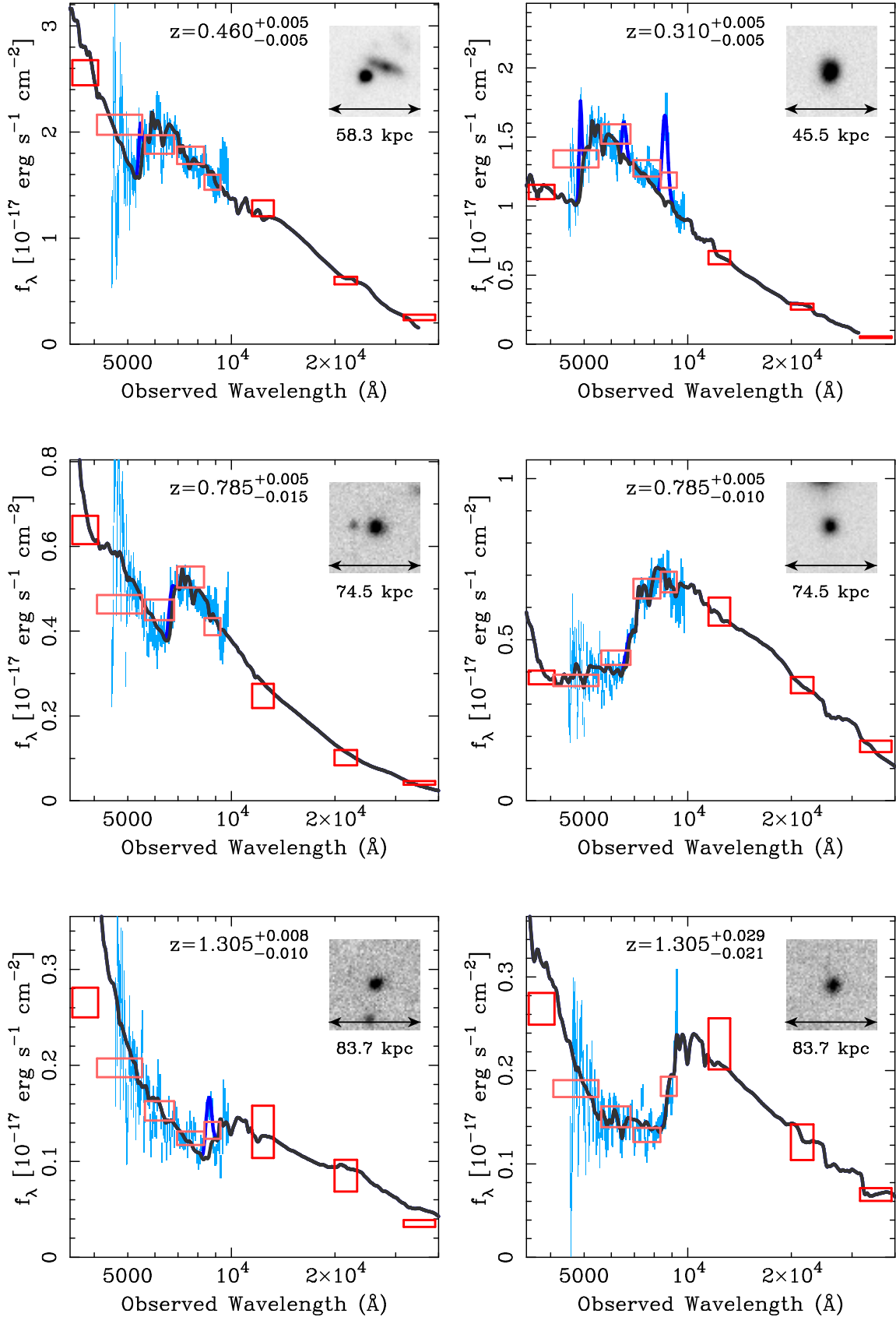


Figure 6. Example SEDs for blue galaxies, along with their CSI redshifts and 95% confidence limits. The IMACS spectra are shown in cyan. The red boxes mark the broadband flux measurements in $ugrizJK_s[3,6]$, noting that the SED fitting was performed using $ugrizJK_s$. The best-fit stellar population models are shown with thick black lines. When the data require emission line components in the fit, these are shown using dark blue. Inset we show the CFHTLS z -band images of the galaxies. In particular, we note the top-left and bottom-left, two galaxies for which broadband photometry alone would be insufficient to provide redshift estimates. Low dispersion spectroscopy is key to isolating Balmer breaks and emission lines in blue galaxies, leading to redshift uncertainties with very little dependence on spectral type.

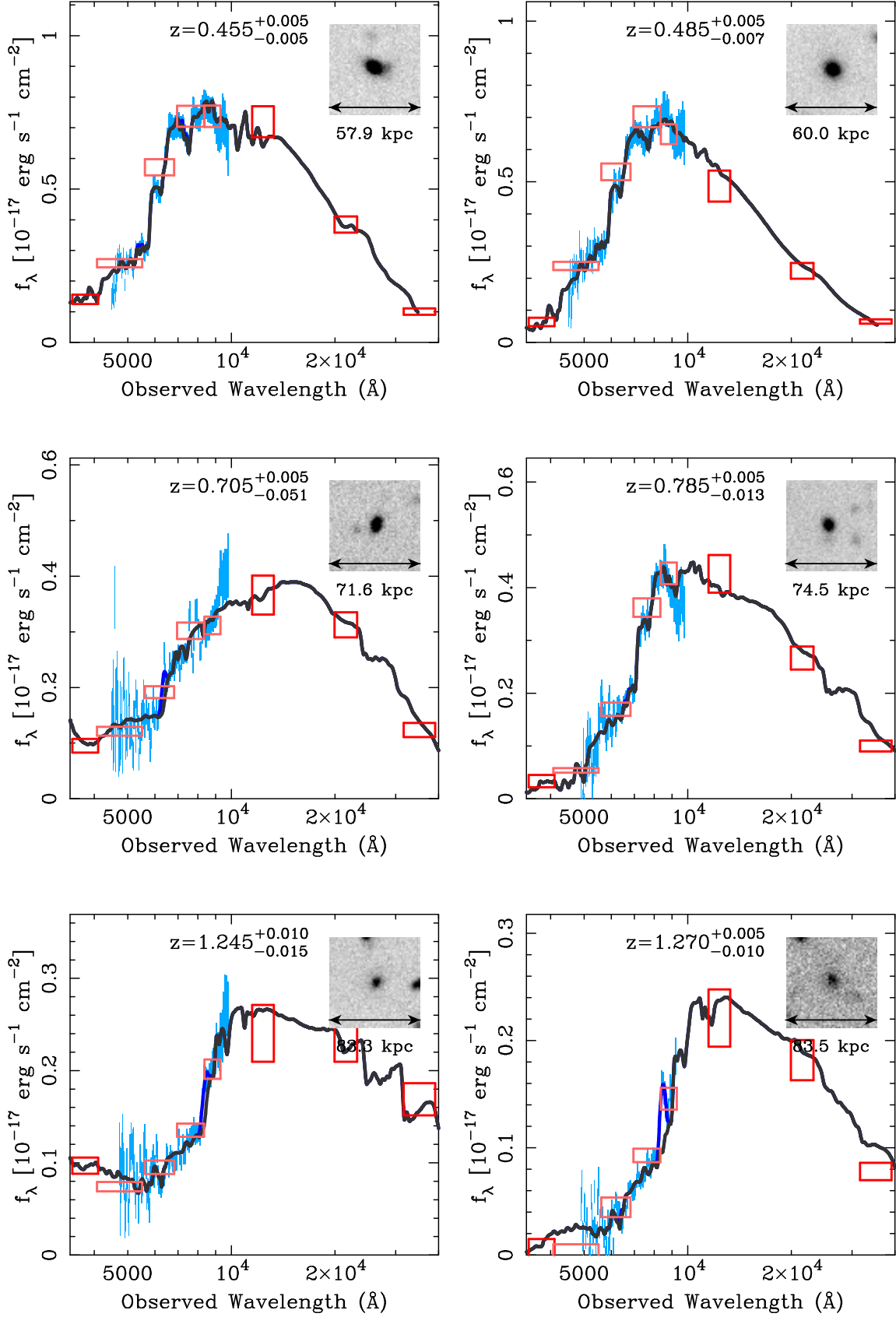


Figure 7. Same as in Fig. 6 but for red galaxies spanning a range of redshifts in CSI. Note the structure in the SEDs traced by both the data and the models outside of the 4000 \AA break.

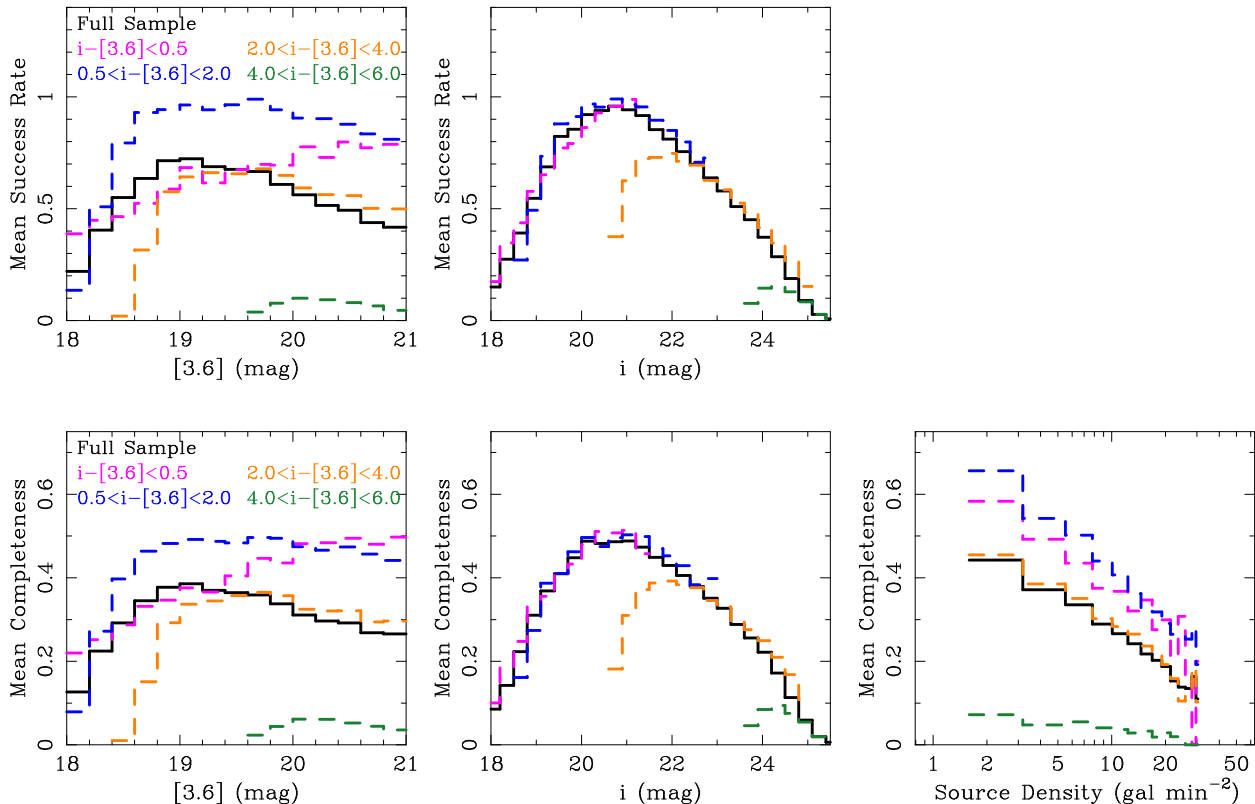


Figure 8. (top) Average success rate as functions of $3.6\mu\text{m}$ and i magnitude, where success rate refers to the fraction of slitlets cut that led to a high quality redshift measurement. (bottom) The average completeness as functions of $3.6\mu\text{m}$ and i magnitude, where completeness is the fraction of galaxies above the $3.6\mu\text{m}$ flux limit within the 5.3 deg^2 area that have a high quality CSI redshift. At a given $3.6\mu\text{m}$ flux, the completeness is a fairly strong function of color, such that it very nearly depends on i -band magnitude alone. We also plot the mean completeness as a function of local source density computed on scales of $2/3 \text{ arcmin}$ in an effort to account the portion of our incompleteness due to slit collisions.

4.6. Redshift Uncertainties

We have three different methods at our disposal for evaluating the accuracy of CSI redshifts: (1) directly comparing our results with several hundred optically-selected high-resolution spectroscopic redshifts in the VVDS sample Le Fevre et al. (2003); (2) deriving uncertainties using the large number of objects with repeat measurements; and (3) employing the Quadri & Williams (2010) pairwise velocity approach, in which galaxy groups and large scale structures mean that large numbers of galaxies lie at the same redshifts, effectively providing repeat redshift measurements of cosmic structures. All three methods give consistent estimates of the redshift uncertainty to $r \sim 25 \text{ mag}$ and/or $z = 1.3$. At fainter magnitudes and higher redshift there is insufficient overlap to empirically characterize the redshift errors using the VVDS. However, to these limits, these checks on our redshift uncertainties all show good agreement.

4.6.1. Comparison with VVDS

In our sample of galaxies with high quality redshifts, there are 400 with VVDS spectroscopic measurements; Figure 9 compares these redshifts. We have visually inspected and verified redshifts of the VIMOS spectra of these objects common to the VVDS and CSI, in a few cases revising VVDS redshifts and quality flags. For VVDS objects flagged as ‘low quality’ (3 & 2), we were not able to verify all redshifts; we nevertheless include

them here, using smaller points in Figure 9.

For the 191 galaxies with high quality VVDS measurements, 91% of the redshifts agree to within $\delta z/(1+z) < 0.02$, with 96% within $\delta z/(1+z) < 0.05$. The standard deviation for this subsample is $\sigma_z/(1+z) = 0.008$ (using $\sigma = 1.48 \times \text{MAD}$ median absolute deviation; Beers et al. 1990). For the 138 with poor quality flags in the VVDS subsample the scatter is $\sigma_z/(1+z) = 0.014$, with 86% agreeing to within $\delta z/(1+z) < 0.05$. In Figure 9 we show the 1σ scatters in different magnitude bins also derived using $\sigma = 1.48 \times \text{MAD}$. Note that these values include a number of galaxies with low quality VVDS redshifts. For galaxies down to the PRIMUS selection limit of $i = 23 \text{ mag}$, the scatter is $\sigma_z/(1+z) = 0.009$. Fainter than $i = 23 \text{ mag}$, the scatter rises to $\sigma_z/(1+z) = 0.025$. For galaxies selected by CSI to be between $1 < z < 1.5$, we find $\sigma_z/(1+z) = 0.033$, though the distribution is non-Gaussian and the subsample largely contains objects with low quality VVDS redshifts.

The comparisons between our redshifts and those made available by the VVDS have allowed us to confirm that our procedures are working well. However, a larger numbers of galaxies is required to accurately characterize redshift uncertainties as a function of magnitude, color, or spectral type. Fortunately, we have two additional tests to help us probe the accuracy of our redshifts.

4.6.2. Uncertainties Derived from Repeat Measurements

The data from individual slit masks were reduced independently, and so repeat measurements can be compared.

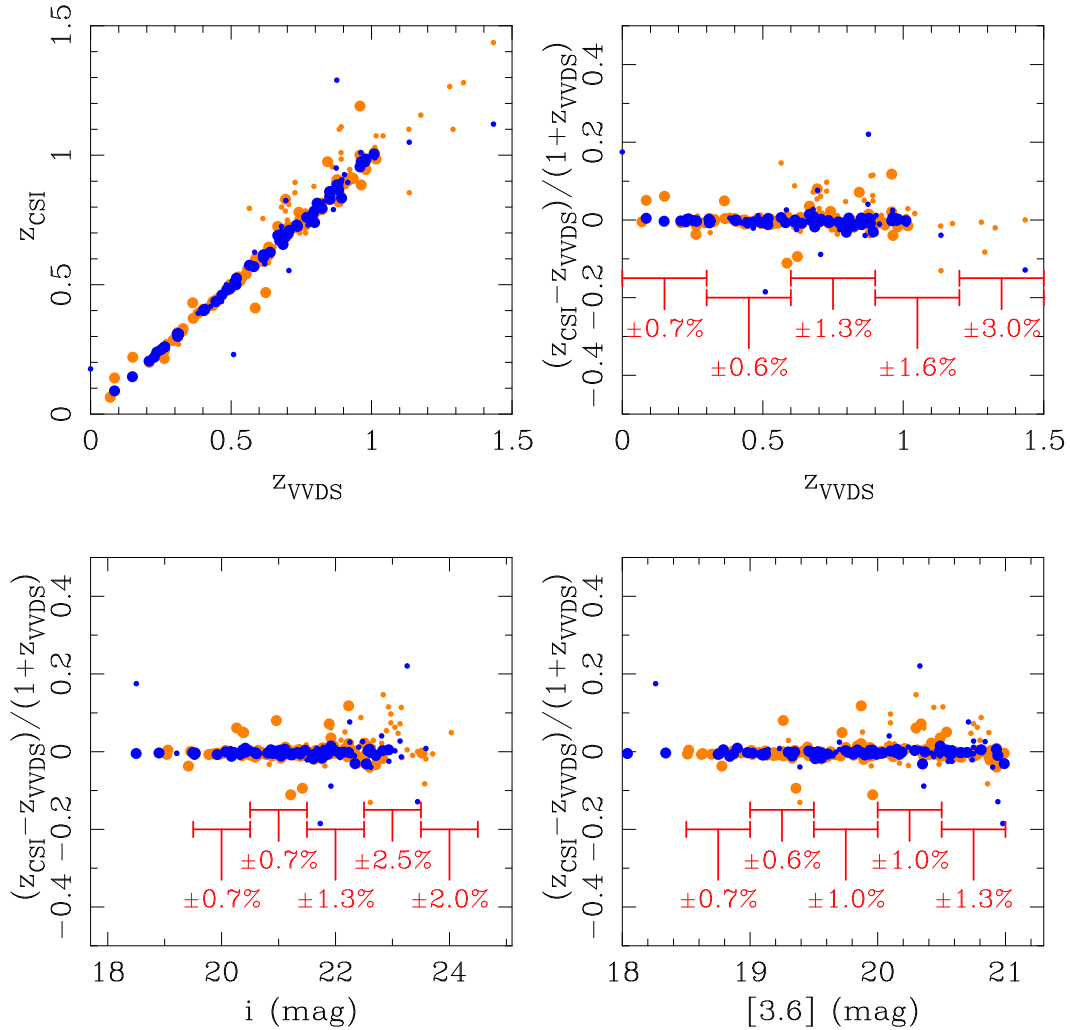


Figure 9. (top left) CSI redshifts plotted against VVDS redshifts with quality flags 3,4,5. Larger symbols indicate higher quality VVDS redshift flags. In orange and blue we show those galaxies observed with the LDP and UDP respectively. (top right) Fraction redshift error vs. VVDS redshift. Numbers shown with bins along the x-axis show the 1σ estimate of the scatter, computed using $\sigma = 1.48 \times \text{MAD}$ (median absolute deviation; Beers et al. 1990). (bottom left) and (bottom right) Fractional redshift error vs. i -band, and $3.6\mu\text{m}$ magnitude. For galaxies with high quality VVDS redshift flags, we find a 1σ scatter of 1% in $\delta z / (1 + z)$, and that for galaxies between $0.7 < z < 1.0$, 94% have fractional redshift errors $\delta z / (1 + z) < 5\%$.

These comprise approximately 20% of the measured redshifts, providing a sample large enough to be analyzed as a function of galaxy properties, such as magnitude, color, stellar mass, or redshift. Without prior constraints or measurements for the derived properties of these objects we adopt the mean of multiple measurements when plotting or analyzing the distributions as functions of redshift. In Figure 10 we plot the 68% fractional redshift differences against redshift, as well as $3.6\mu\text{m}$ and i -band magnitudes. As a function of redshift the half-width of the 68% confidence is 0.9% at $0.6 < z < 0.9$, 2.2% for $0.9 < z < 1.2$. As can be seen in the third panel, the width of the distribution is a stronger function of optical magnitude than near-IR magnitude because our SED fitting is dominated by the IMACS spectroscopy. Currently, we find $\sigma = 3\%$ at $22.5 \text{ mag} < i < 24 \text{ mag}$, and $\sigma = 5\%$ at $24 \text{ mag} < i < 25.2 \text{ mag}$. Planned refinements in the pipeline are expected to improve the fidelity of the extracted spectra for such faint sources as the CSI Survey progresses.

The redshift uncertainties are dissected further in Fig-

ure 11 by breaking up the sample into three redshift ranges and plotting against S/N ratios of the IMACS spectra, stellar mass, star formation activity, and rest frame $u - g$ color. From these panels one can see that the redshift errors are not strongly correlated with spectral type or color, unlike the typical dependencies seen in photometric redshifts. There is a rather small, subtle dependence on spectral type: quiescent galaxies (those with a negligible specific star formation rate and hence strong Balmer/4000Å breaks) and strongly starforming galaxies have the greatest precision, while galaxies with modest or intermediate SFR have degraded redshift precision. Weak [OII]3727 Å emission at high redshift and observed at low resolution can appear blended with the 4000Å break and produce spectra that are reasonably well fit by an SED with a Balmer break and no [OII]3727 Å. More specifically, [OII]3727 Å is imperfectly correlated with the SFR inferred from the stellar continuum, leading to an additional uncertainty in the redshifts at the $\sim 1 - 2\%$ level, depending on the S/N ratio of the spectra, and even when not particularly sta-

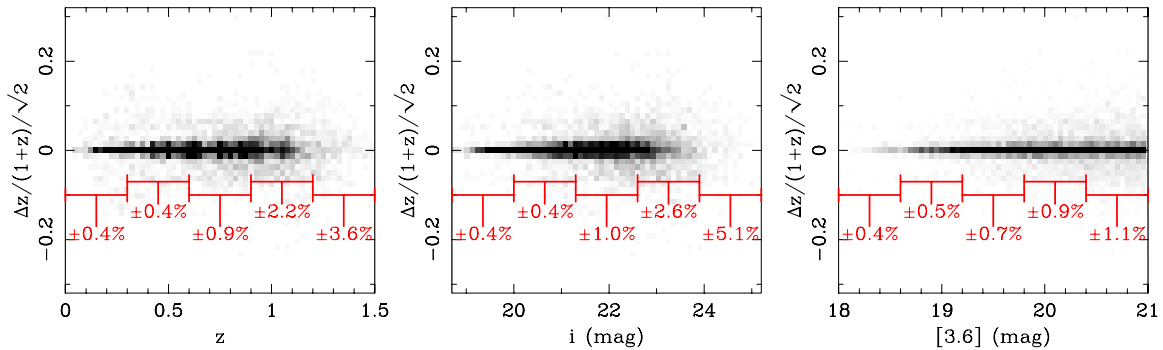


Figure 10. Fractional redshift differences between repeat measurements, scaled by $\sqrt{2}$, as functions of redshift, $3.6\mu\text{m}$ magnitude, and i -band magnitude. For example, at $0.6 < z < 0.9$, the half-width of the 68% confidence interval is $\sigma = 0.9\%$. At $0.9 < z < 1.2$ we find $\sigma = 2.3\%$. As can be seen in the third panel, the width of the distribution is a stronger function of optical magnitude than near-IR magnitude, because our SED fitting is dominated by the IMACS spectroscopy. We find $\sigma = 2.6\%$ at $22.5 \text{ mag} < i < 24 \text{ mag}$, and $\sigma = 5\%$ at $23.5 \text{ mag} < i < 24.8 \text{ mag}$.

tistically significant. This effect is substantially less pronounced for UDP data, where the higher resolution of the disperser shifts the wavelength of such $[\text{OII}]3727\text{\AA}$ confusion farther to the red. This power of the higher resolution UDP is illustrated in the last SED of Figure 6, in an old galaxy at $z = 1.27$ with $[\text{OII}]3727\text{\AA}$ line emission (likely a LINER, e.g. Lemaux et al. 2010). Again, this problem with low resolution spectroscopy is only important for “green” galaxies; the bulk of the galaxy population, lying in the blue cloud and red sequence (with strong $[\text{OII}]3727\text{\AA}$ and Balmer breaks respectively), is unaffected.

While the abundance of repeat spectroscopic measurements has allowed us to characterize the redshift uncertainties, repeated spectra of any given object are fine-tuned with the same broadband photometry as described in Section 4.2. For some galaxies this can in principle introduce artificially tight correlations between the repeat spectroscopic measurements. Presumably, this issue becomes a serious problem only if the broad-band photometry is allowed to have greater weight in the likelihood analysis. This never occurs in our procedures, in particular because the number of data points in the UDP and LDP spectra far exceed the number of photometric bands. Even when the S/N ratios of the spectra are low, binning these data over the photometric bandpasses yield S/N ratios that still exceed what obtains from the photometry for those fainter galaxies. Even with these reasons to trust the analysis of the repeat measurements, we employ yet another means to assess the redshift errors in the next section.

4.6.3. Uncertainties from Pairwise Velocity Distributions

Because galaxies largely exist in close pairs, in groups, in clusters, and in even larger coherent structures, all of which have velocity widths smaller than the redshift errors we expect in our data and analysis, the distribution of redshift errors can be inferred statistically from the distribution of pairwise redshift differences in a given sample. This technique was first explored and described by Quadri & Williams (2010) in an effort to derive the redshift uncertainties in photometric redshift surveys, where a lack of repeat measurements and limited templates can hamper one’s ability to estimate uncertainties. Any methodology relying explicitly on clustering requires dense spatial sampling in order to extract a high

S/N signal from the pairwise velocity histograms. While photometric redshift surveys, by definition, result in the highest possible spatial sampling, the spatial sampling of CSI is limited by slit collisions. This limits the number of galaxy pairs available to perform this analysis, compared to what would be obtained in a purely photometric redshift survey.

We divided our sample into subsets based on r -band magnitude and redshift and constructed pairwise velocity histograms. For the subsamples based on magnitude, we used those galaxies brighter than a given bin as a reference set, assuming those galaxies have more precise redshifts. While Quadri & Williams (2010) chose to randomize the positions in their dataset to correct for close pairs that arise only in projection, we opted to randomize the galaxy velocities since our slit-placement constraints lead to nontrivial spatial dependencies. Care was taken to properly normalize the histograms derived from the randomized distributions, as the number of galaxies in them, by definition, is too large by the number of galaxies within coherent velocity structures. Because this number cannot be precisely defined *a priori*, it must be deduced from the data — from the wings of the histograms. We made several realizations to reduce the Poisson noise imposed by the randomization process.

The results of these experiments are shown in Figure 12 as the red histogram. Overplotted are the 1σ confidence limits on our redshifts, shown in blue, and computed by dividing the 95% confidence limits by four. The green filled circles are the expected standard deviations of the pairwise velocity histograms for galaxies with redshift uncertainties shown in blue. Overall the Quadri & Williams (2010) method has reinforced the validity of the redshift uncertainties derived from our generalized likelihood analysis down to faint magnitudes, and from our comparisons to the relatively bright VVDS sample.

This result should be of general interest, since the Quadri & Williams (2010) method was in part devised to remedy the deficiency that photometric redshift surveys do not provide repeat measurements of a given galaxy. However, any spatially dense survey will provide repeat measurements of (relatively) cold cosmic structures, so the Quadri & Williams (2010) methodology remains a valuable technique for any spatially dense spectroscopic or photometric redshift survey — any survey where one does not have repeat observations with which to charac-

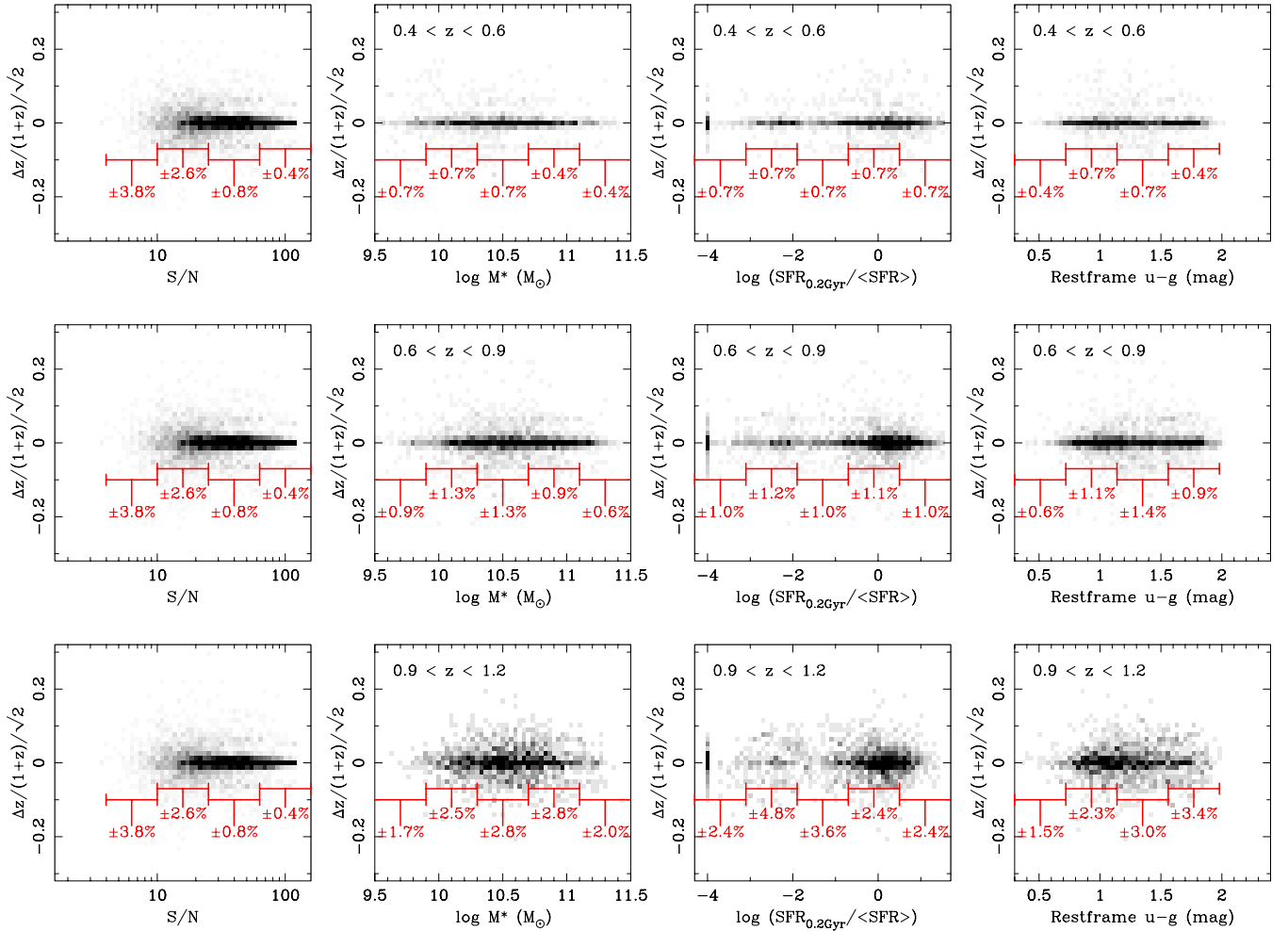


Figure 11. Fractional redshift differences between repeat measurements, scaled by $\sqrt{2}$, as functions of S/N ratio (75th percentile of the prism spectra), stellar mass, relative star formation activity, and restframe $u-g$ color. There is very little dependence of the redshift errors on spectral type or color, unlike what is typically seen for photometric redshifts.

terize uncertainties empirically.

Based on these three methods, we conclude that our random redshift uncertainties have been reliably characterized, and also that systematic uncertainties appear to be minimal. In particular we stress that our redshift errors are not strongly dependent on relative star formation activity, spectral type, or color. As discussed by Quadri et al. (2012), redshift errors that are strongly correlated with spectral type will bias estimates of local galaxy density if care is not taken to ensure that velocity windows or velocity linking lengths can encompass both red and blue galaxies with equal probability. Given CSI’s primary goal of characterizing galaxy properties as a function of environment, the relative insensitivity of our redshift errors on spectral type is a crucial point.

5. DISCUSSION

We conclude our discussion of the survey by presenting a broad overview of the CSI sample, by tracing basic properties of these Spitzer-selected galaxies over time. We specifically highlight the selection limits in order to give the reader a better sense of the depth of the sample in redshift, luminosity, and stellar mass.

Figure 13 shows the distribution of (top) rest frame B -band magnitude and (bottom) stellar mass as func-

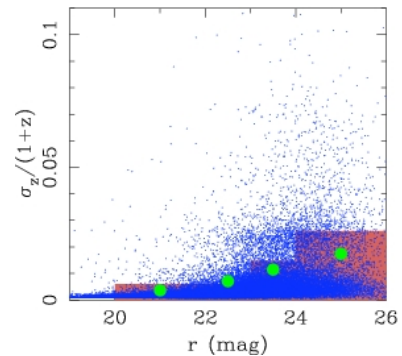


Figure 12. A comparison of the redshift uncertainties derived from the likelihood functions with the mean uncertainty as a function of magnitude derived from the pairwise velocity histogram method of Quadri & Williams (2010). In blue we plot 1σ redshift uncertainties for the individual galaxies. In green we plot the expected standard deviation of the pairwise velocity histograms from the blue points. The red shaded bars trace the measured standard deviations from the pairwise velocity histograms as functions of magnitude. The comparison is quite good, suggesting that the uncertainties from our redshift fitting procedures are robust.

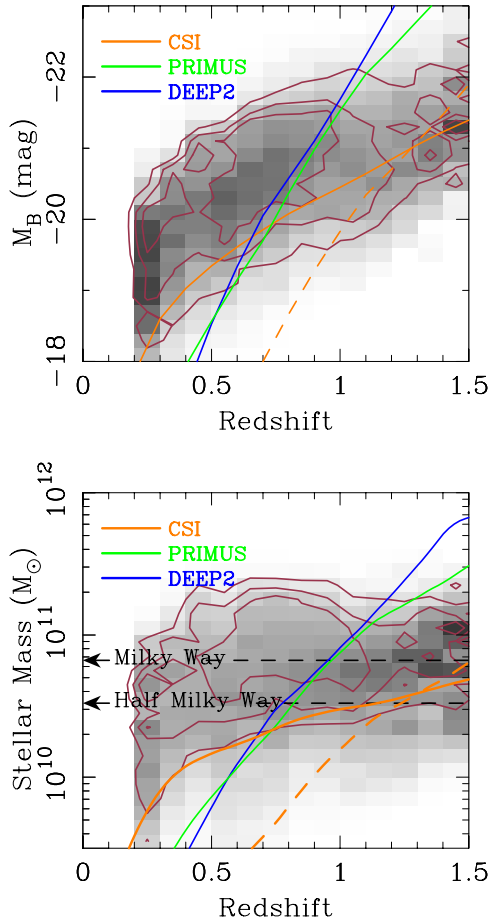


Figure 13. The distribution of our $3.6\mu\text{m}$ -selected galaxies in (top) restframe B -band magnitude and (bottom) stellar mass, as functions of redshift, where we have normalized the distribution at each redshift by the number counts in each redshift bin. The green and blue lines indicate the approximate loci for old stellar populations at the limits of the PRIMUS and DEEP2 surveys. In orange, we show the CSI selection limit of $3.6\mu\text{m} = 21$ mag (solid) and the effective optical limit of $i = 24.7$ mag (dashed). The maroon contours trace the distribution of “quiescent” galaxies, as selected by their restframe $(U - V)$ and $(V - J)$ colors (Williams et al. 2009). Selection in the near-IR has ensured that CSI does not *a priori* exclude the bulk of passively evolving systems at $z \gtrsim 1$. Meanwhile, the observing strategy, reductions, and first analysis of the data enable CSI to reach more than a magnitude fainter in the optical than DEEP2 or PRIMUS.

tions of redshift. The dark red contours specifically outline the distribution of quiescent galaxies, as selected by their restframe $U - V$ and $V - J$ colors (Williams et al. 2009). The CSI $3.6\mu\text{m}$ flux limit is shown by the solid orange lines, along with our effective optical limit of $i \approx 24.7$ mag as dashed orange lines. This i -band limit, where our spectroscopic completeness falls below $1/3$ of the maximum (of 50% at $i = 21$ mag, see Fig. 8), dominates over the IRAC selection at $z > 1.2$. In these plots, the sample becomes irreparably incomplete for galaxies at masses or magnitudes below the lines. These figures show that the goal of producing a large, cosmologically representative set of galaxies back to $z \approx 1.5$ is being achieved. CSI is probing galaxies with the present day stellar mass of the Milky Way to a time when the universe was 9 Gyr younger than today and without explicitly excluding galaxies with low M/L ratios.

For comparison, we plot the DEEP2 and PRIMUS

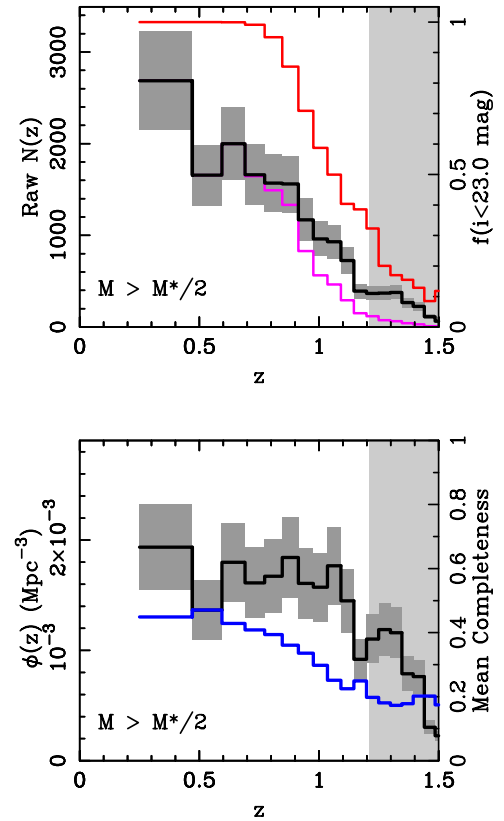


Figure 14. (top) Distributions of high quality redshifts for galaxies more massive than half that of the Milky Way. The redshift bins are defined by a constant comoving volume in which cosmic variance is $\sim 20\%$ for red galaxies (dark gray boxes; Somerville et al. 2004). The apparent decline in $N(z)$ above $z = 0.7$ is due to an increase in spectroscopic incompleteness (i.e. a declining success rate, see the bottom panel). (bottom) Applying completeness corrections, we convert $N(z)$ to the comoving number density of galaxies as a function of redshift. We plot the mean completeness as a function of redshift in blue. The light gray shaded region beyond $z = 1.2$ in the right-hand panel shows approximately where the faint optical magnitude limit of the current analysis cuts the sample on the red sequence (see Figure 1).

magnitude limits of $r = 24.1$ mag and $i = 23.0$ mag using the blue and green lines, respectively. These surveys can probe unbiased samples down to the stellar mass of the Milky Way back to $z = 0.9$, and half the mass of the Milky Way to $z = 0.75$. CSI’s additional reach to $z = 1$ for galaxies with half the mass of the Milky Way may only reach 1 Gyr farther back in cosmic time, but the comoving volume covered within a constant area on the sky is nearly double that of PRIMUS. Such gains in sensitivity highlight the importance of an infrared selection in crafting a minimally unbiased picture of galaxies since $z = 1.5$.

Figure 14 (top) shows the distribution of high quality redshifts for galaxies with stellar masses $M > M^*/2$, using redshift bins estimated to have constant cosmic variance of $\sim 20\%$ (Somerville et al. 2004, shown in dark gray). A large fraction of the decline in $N(z)$ is due to our declining success rates and completeness at fainter optical magnitudes (as shown by the blue lines in the bottom panel). As can be seen Figure 13, however, selection at brighter optical limits, however, would have dramatically exacerbated the incompleteness. Cutting at $i = 23$ mag (the PRIMUS magnitude limit) would have eliminated

$\sim 50\%$ of those galaxies at $z = 1$ in CSI. Selection at those wavelengths that more closely trace stellar mass, and a methodology for measuring redshifts that does not depend crucially on the presence of emission lines at faint magnitudes, ensures, at least *a priori*, that the resulting samples are free from bias against galaxies with low M/L ratios at fixed mass.

We have applied completeness corrections and converted our $N(z)$ figures to estimates of the comoving number densities of galaxies as functions of redshift in this stellar mass range and plot them in the bottom panels. The dark gray, again, shows the estimated cosmic variance of $\sim 20\%$, which dominates the uncertainties (\sqrt{N}/N is small). The light gray shaded region shown at high redshift in the bottom right indicate redshifts where our faint magnitude limits impinge on the low mass end of this subsample and the selection biases become important. The mean of our completeness estimates as functions of redshift are plotted in blue.

Detailed analysis of the evolution in number densities of galaxies over cosmic time is beyond the scope of this first paper, which has primarily focused on the motivation behind the survey and discussion of the handling of the data. However, Figure 14 reinforces what previous deep surveys covering smaller fields-of-view have found: fairly modest evolution in the number densities of normal galaxies since $z = 1$ (Drory et al. 2009; Marchesini et al. 2009; Ilbert et al. 2010, e.g.). In subsequent publications from the Carnegie-Spitzer-IMACS Survey, we will begin dissecting the dataset in order to identify galaxy groups and trace the evolution of the mass function of such groups since $z = 1$ (Williams et al. 2012), and begin characterizing the star formation activity and histories of galaxies in groups of different mass scales as a function of time.

6. SUMMARY

We have described the methodology and initial data of an ambitious new survey of approximately 2×10^5 galaxies over a volume that encompasses the last 9 Gyr of cosmic history. By selecting a sample at $3.6\mu\text{m}$ from Spitzer-IRAC, the CSI survey is the most uniform to-date in terms of limiting mass as a function of redshift, and will ultimately cover an unbiased volume comparable to SDSS but at $0.5 < z < 1.5$. The power of the *IMACS* spectrograph with low-resolution prisms allows us to survey large volumes efficiently and with sufficient spectral resolution to detect large-scale structure and to measure emission lines from strongly star-forming galaxies and AGN. CSI provides comparable redshift accuracies for red sequence and blue cloud galaxies; a significant advantage compared to many broadband photometric—and even some spectroscopic—studies. By combining our low-resolution spectrophotometry with extended broadband photometry and sophisticated SED modeling, CSI bridges the gap between surveys that are deep enough to probe galaxies below M^* but are small in sample size and volume, and those large-sample, large-volume surveys that do not reach typical, Milky Way-like galaxies that are the main event in the history of cosmic evolution. In forthcoming papers we will update with more detail what we have learned from the first batch of CSI survey data.

Once the three survey fields of CSI have been com-

pleted at the end of 2012, we will have probed a volume equivalent to the SDSS, enabling a vast number of studies of distant galaxies. One of the highest priority goals will be to take advantage of this volume to simultaneously measure the evolution of the group mass function (e.g. Williams et al. 2012), and the dependence of star formation on environment (e.g. Kelson et al. 2012). By doing so CSI will uncover the extent to which the growth in the number density of passive galaxies over the past 2/3 of the lifetime of the universe can be attributed to group-related processes such as, for example, galaxy-galaxy interactions (leading to differential number density evolution between groups and galaxies), and/or a decrease in the available fuel for on-going star formation (leaving galaxy number densities unchanged). Given that most galaxies in groups are “red and dead” even at $z \sim 1$ (Kelson et al. 2012), the mass selection, high spectral coverage, and color-insensitive redshift accuracy of CSI will all be critical elements in characterizing relatively poor groups at high redshift. Subsequent CSI analyses will also focus on, for example, AGN and any connections to group and/or host galaxy properties, on differences between centrals and satellites (e.g. Berlind & Weinberg 2002; Weinmann et al. 2006; van den Bosch et al. 2007), and on merger rates (e.g. Williams et al. 2011) as functions of environment.

7. ACKNOWLEDGMENTS

D.D.K. expresses his appreciation to his co-investigators for their patience. The whole team also appreciates the enormous contributions of the Carnegie Institution for Science to the project, from the new disperser to the generosity of the Time Assignment Committee. We are grateful to NOAO for its contributions and to the astronomical community for its awarding of survey status to CSI in 2009. R.J.W. also gratefully acknowledges support from NSF Grant AST-0707417. Based, in part, on observations obtained with MegaPrime/MegaCam, a joint project of CFHT and CEA/DAPNIA, at the Canada-France-Hawaii Telescope (CFHT) which is operated by the National Research Council (NRC) of Canada, the Institut National des Science de l’Univers of the Centre National de la Recherche Scientifique (CNRS) of France, and the University of Hawaii. This work is based in part on data products produced at TERAPIX and the Canadian Astronomy Data Centre as part of the Canada-France-Hawaii Telescope Legacy Survey, a collaborative project of NRC and CNRS. This publication makes use of data products from the Two Micron All Sky Survey, which is a joint project of the University of Massachusetts and the Infrared Processing and Analysis Center/California Institute of Technology, funded by the National Aeronautics and Space Administration and the National Science Foundation

REFERENCES

- Abraham, R. G., et al. 2004, *AJ*, 127, 2455
- Autry, R.G. et al. 2003, *SPIE*
- Baldry, I. K., Balogh, M. L., Bower, R. G., Glazebrook, K., Nichol, R. C., Bamford, S. P., & Budavari, T. 2006, *MNRAS*, 373, 469
- Beers, T. C., Flynn, K., & Gebhardt, K. 1990, *AJ*, 100, 32
- Bell, E. F., & de Jong, R. S. 2001, *ApJ*, 550, 212

- Berlind, A. A., & Weinberg, D. H. 2002, *ApJ*, 575, 587
Bertin, E., & Arnouts, S. 1996, *A&AS*, 117, 393
Bruzual, G., & Charlot, S. 2003, *MNRAS*, 344, 1000
Coil, A. et al. 2010, *astro-ph*
Cooper, M. C., et al. 2010, *MNRAS*, 409, 337
Cuillandre, J.-C., & Bertin, E. 2006, *SF2A-2006: Semaine de l'Astrophysique Francaise*, 265
Dressler, A. 1980, *ApJ*, 236, 351
Dressler, A., Bigelow, B., Hare, T., et al. 2011, *PASP*, 123, 288
Drory, N., Bundy, K., Leauthaud, A., et al. 2009, *ApJ*, 707, 1595
Faber, S. M., et al. 2007, *ApJ*, 665, 265
Gilbank, D. G., Baldry, I. K., Balogh, M. L., Glazebrook, K., & Bower, R. G. 2010, *MNRAS*, 405, 2594
Glazebrook, K., & Bland-Hawthorn, J. 2001, *PASP*, 113, 197
Halliday, C., Daddi, E., Cimatti, A., et al. 2008, *A&A*, 479, 417
Högbom, J. A. 1974, *A&AS*, 15, 417
Horne, K. 1986, *PASP*, 98, 609
Huber, P. J. *Robust Statistics*. John Wiley & Sons, New York, 1981
Huchra, J.P., & Geller, M.J., 1982, *ApJ*, 257, 423
Ibort, O., Salvato, M., Le Floch, E., et al. 2010, *ApJ*, 709, 644
Kauffmann, G., White, S. D. M., Heckman, T. M., Ménard, B., Brinchmann, J., Charlot, S., Tremonti, C., & Brinkmann, J. 2004, *MNRAS*, 353, 713
Kelson, D. D., Illingworth, G. D., van Dokkum, P. G., & Franx, M. 2000, *ApJ*, 531, 184
Kelson, D. D., et al. 2012, *ApJ*, in prep
Kewley, L. et al. 2004
Knobel, C. et al. 2009, *ApJ*, 697, 1842
Le Fevre, et al. 2003
Lemaux, B. C., Lubin, L. M., Shapley, A., et al. 2010, *ApJ*, 716, 970
Lilly, S. et al. 2007
Lonsdale, C. J., et al. 2003, *PASP*, 115, 897
Maraston, C. 2005, *MNRAS*, 362, 799
Marchesini, D., van Dokkum, P. G., Förster Schreiber, N. M., et al. 2009, *ApJ*, 701, 1765
McMillan, P. J. 2011, *MNRAS*, 414, 2446
Patel, S. G., Kelson, D. D., Holden, B. P., Illingworth, G. D., Franx, M., van der Wel, A., & Ford, H. 2009, *ApJ*, 694, 1349
Patel, S. G., Holden, B. P., Kelson, D. D., Illingworth, G. D., & Franx, M. 2009, *ApJ*, 705, L67
Patel, S. et al. 2011, *ApJ*, submitted
Pozzetti, L., Bolzonella, M., Zucca, E., et al. 2010, *A&A*, 523, A13
Quadri, R. F., & Williams, R. J., (2010), *ApJ*, 725, 794
Quadri, R. F., Williams, R. J., Franx, M., & Hildebrandt, H. 2012, *ApJ*, 744, 88
Skrutskie, M. F., et al. 2006, *AJ*, 131, 1163
Sorba, R., & Sawicki, M. 2010, *ApJ*, 721, 1056
Somerville, R.S, et al. 2004, *ApJ*, 600, L171
Springel, V. et al. 2005, *Nature*, 435, 629
Surace, J. et al. 2005, preprint
van den Bosch, F. C., Yang, X., Mo, H. J., et al. 2007, *MNRAS*, 376, 841
Weinmann, S. M., van den Bosch, F. C., Yang, X., & Mo, H. J. 2006, *MNRAS*, 366, 2
Williams, R. J., Quadri, R. F., Franx, M., van Dokkum, P., & Labbé, I. 2009, *ApJ*, 691, 1879
Williams, R. J., Quadri, R. F., & Franx, M. 2011, *ApJ*, 738, L25
Williams, R. J., et al. 2012, *ApJ*, in prep
Willmer, C. N. A., et al. 2006, *ApJ*, 647, 853
Zhang, Z. 1997, *Image and Vision Computing*, 15, 59